Constrained Stochastic State Estimation for 3D Shape Reconstruction of Catheters and Guidewires in Fluoroscopic Images

Raffaella Trivisonne, Erwan Kerrien, Stéphane Cotin

Constrained Stochastic State Estimation for 3D Shape Reconstruction of Catheters and Guidewires in Fluoroscopic Images Submitted for Publication

Raffaella Trivisonne, Erwan Kerrien, Stéphane Cotin
MIMESIS, , Inria Nancy - Grand Est.
MAGRIT , Inria Nancy - Grand Est.

ABSTRACT

Minimally invasive fluoroscopy-based procedures are the gold standard for diagnosis and treatment of various pathologies of the cardiovascular system. This kind of procedures imply for the clinicians to infer the 3D shape of the device from 2D images, which is known to be an ill-posed problem. In this paper we present a method to reconstruct the 3D shape of the interventional device, with the aim of improving the navigation. The method combines a physics-based simulation with non-linear Bayesian filter. Whereas the physics-based model provides a prediction of the shape of the device navigating within the blood vessels (taking into account non-linear interactions between the catheter and the surrounding anatomy), an Unscented Kalman Filter is used to correct the navigation model using 2D image features as external observations.

The proposed framework has been evaluated on both synthetic and real data, under different model parameterization, filter parameters tuning and external observations data-sets. Comparing the reconstructed 3D shape with a known ground truth, for the synthetic data-set, we obtained an average 3D Hausdorff distance of 0.07 ± 0.37 mm; the 3D distance at the tip equal to 0.021 ± 0.009 mm and the 3D mean distance at the distal segment of the catheter equal to 0.02 ± 0.008 mm. For the real data-set, the obtained average 3D Hausdorff Distance was of 0.95 ± 0.35 mm, the average 3D distance at the tip is equal to 0.7 ± 0.45 mm with an average 3D mean distance at the distal segment of 0.7 ± 0.46 mm. These results show the ability of our method to retrieve the 3D shape of the device, under a variety of filter parameterizations and challenging conditions: errors on the friction coefficient, ambiguous views and non-linear complex phenomena such as stick and slip motions.

Keyword: Constrained Unscented Kalman Filter, Physics-based simulation, Catheter Reconstruction, Endovascular Intervention, Computer Aided Suregery

1 Introduction and context

Image-guided minimally invasive procedures have become the gold standard for diagnostic or treatment of many pathologies. Whereas static images, such as CT or MRI scans, are rather used for surgical planning or timely assessment of the surgical instrument position, real-time imaging, such as fluoroscopy, provides the visual feedback necessary for all interventional radiology procedures. The limitations of fluoroscopy based procedures are mainly associated with dose absorption and the intrinsic properties of X-rays images. Indeed, a contrast medium often needs to be injected in order to highlight the different overlaying anatomical structures, such as blood vessels. Fluoroscopic images are also affected by a lack of depth perception proper to all 2D projected images, which has been identified as one of the most important factors affecting clinical performance [1]. In this sense, providing in real-time a 3D view of interventional devices (such as catheters or guidewires) could improve the intervention, reduce procedure time and facilitate the navigation. However, retrieving the 3D shape of an object from 2D features is an ill-posed problem: due to missing depth information, several 3D shapes may correspond to a given 2D configuration (Fig. 1). For endovascular interventions, one possible solution is to use bi-plane imaging systems in order to overcome the ambiguity of 2D images. Contrary to what occurs with stereoscopic cameras in laparoscopic procedures, there is no risk of occlusion in fluoroscopic images. However, the wide baseline and the lack of texture makes image features extraction and matching more difficult. Several works present methods to reconstruct the device in 3D from 2D

images acquired with bi-planar systems [2, 3], but such equipment is not very common in current practice. Given that single plane systems are more extensively used in clinical routine, in this work we propose a method to reconstruct, online and in 3D, the interventional device from 2D monocular fluoroscopic images. In this context, previous methods may be classified as

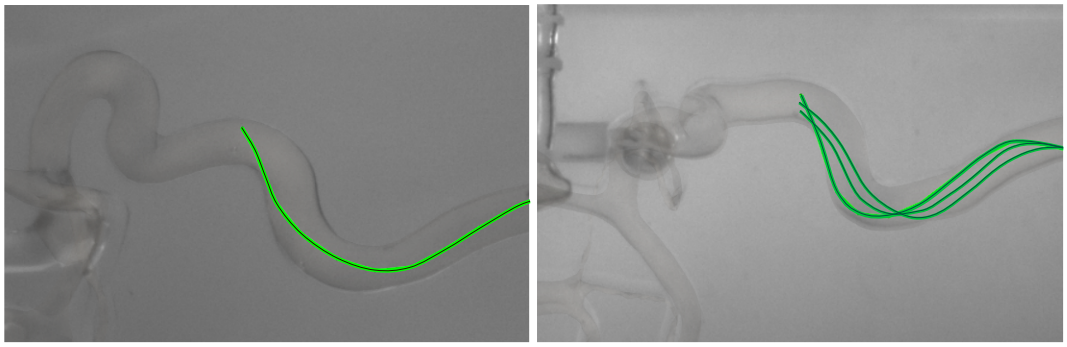

(a) Side view (b) Top view

Fig. 1. **2D-3D Registration**. Ill-posed problem: several 3D shapes may correspond to the same 2D configuration. Catheter shapes can be seen as different in a top view (b) but may project onto the same curved line in a side view (a).

follows: reconstruction methods exploiting position or shape sensors, computer vision methods based on the use of images and geometric models, and reconstruction methods combining fluoroscopic images and a physics-based model of the device.

For the methods using external sensors, the general idea is to embed an external sensor into the instrument, in order to have a three-dimensional knowledge on the position of the tip or other parts of the device. Condino et al. [4] proposed to use electro-magnetic (EM) tracking in combination with occasional intra-operative CTA. Similarly, in [5] the EM data are completed with ultrasonography to update pre-operative CT data. However, image acquisition and registration are time consuming and cannot be performed frequently enough to guarantee consistency between the virtual and real anatomies. EM trackers were also combined in [6] with a robotic catheterization system, providing a 3D instrument position and orientation visualization instead of the classic 2D fluoroscopic view. Although embedded trackers can give a rather precise location of the catheter, they allow only for a very partial reconstruction of the device and a full shape cannot be retrieved. In addition, their embedding on the interventional device implies significant changes on the clinical workflow and restricts clinical applications. EM Localization errors may further increase in the clinical environment of an operating room, where interactions with ferromagnetic materials cannot be neglected.

Computer vision methods aim at retrieving the 3D reconstruction of objects from 2D images. Given the illposedness of the problem, some hypotheses need to be made in order to restrict the space of possible solutions. In the case of an interventional device, it is assumed to lay inside the vessel surface and regularization constraints are applied to the geometric model and its deformations. Authors in [7], propose to constrain the reconstructed catheter to match the vessel centerline. Such regularization criteria lead to shapes that do not perfectly match reality. In particular, aligning with the centerline precludes from reproducing any contacts between the device and the vessel surface, whereas they occur very frequently, especially in curved vessels. In [8] 3D device reconstruction is defined as a smooth curve that both lies within the blood vessels and projects on the guidewire segmented in the images. The curve smoothness and continuity are ensured with a set of priors, including here again a constraint to stay close to the vessel centerline. Ambiguous cases are not handled and left for the clinician to interpret. Using a particle filter, Brückner et al. [9] combines the 3D geometric model of the vessels with the back-projection of 2D features, creating a 3D probability distribution of the wire positions which is recursively propagated. A spline shape model with maximum length and minimum curvature are priors set to regularize the maximum a posteriori solution. Despite good results, the purely geometric model of the catheter would not ensure a correct reconstruction of the 3D shape when dealing with ambiguous views of the surgical scene (i.e. the catheter moving along the direction of the X-ray detector optical axis or existing overlapping vessels).

All these reconstruction methods rely on geometric prior models of the shape of the catheter and cannot guarantee a reliable reconstruction, in particular under ambiguous views. Moreover the device motion is not modeled, which can make 2D-3D data association, and thereafter reconstruction fail, especially after sudden modifications of the catheter's shape (e.g. following a contact with the surrounding anatomy).

More sophisticated modeling of the device, like a physics based approach, could provide a better description and overcome the above limitations. In [10] we proposed a constrained shape-from-template method combining a physics-based model of the catheter with 2D image features through a constrained approach using Lagrange multipliers. No interactions with the surrounding anatomy were taken into account during the navigation of the catheter, whereas device motion was

entirely driven by the detected image features. Device reconstruction was demonstrated in simple cases but not under ambiguous scenarios, such as anatomy occlusions or partial views. In addition, uncertainties on mechanical characterization of the device, as well as noise on external observations were taken into account only through empirical parameters.

Given the aforementioned approaches, multiple sources of information need to be combined to retrieve a reliable reconstruction of the device: a shape model (physics-based or geometric, including motion and deformation), constraints (contacts with surrounding vessels), and information on the current state of the device (projective 2D from image features, 3D from position or shape sensors). All of the above are prone to be tainted with errors. Recursive Bayesian estimation methods have been investigated to handle those various sources of error. They allow to retrieve the most likely state of a system, described by a process model and observed through external measurements, potentially affected by noise. In [11], a catheter insertion model is combined with 3D positions measured by external EM sensors through an Extended Kalman Filter (EKF). The filter enables to manage both noisy measurements of EM trackers and potential inaccuracies of the catheter insertion model. In a more general computer vision context, sensor-less methods have been proposed to recover the 3D shape of a deforming non-rigid object from a monocular sequence. In particular Finite Element (FE) models enable to implement sophisticated priors on the shape to capture realistic deformations while being robust to occlusions [12, 13]. It has been recently shown how a FE model could be leveraged in an EKF framework to achieve online reconstruction [14]. Two hypotheses are necessary for this method: they assume to know the deformation modes of the surface and they suppose to detect and track some to 2D features, whose correspondences with 3D points of the FE model are assumed to be known. The FE model, driven by the 2D detected features, capture elastic deformations of the surface but it does not provide any information about the dynamic behavior of the object; contacts and collision are not taken into account, whereas only fixed physical constraints can be included in the model. In addition, such framework could not directly fit our specific problem of catheter reconstruction, as a surface FE model cannot be applied to a curved shape like the interventional device.

2 Method

The main aim of our work is to reconstruct the 3D shape of the interventional device from 2D single-view fluoroscopic images. To this end, we propose a finite element (FE) model reproducing the navigation within blood vessels through a constrained physics-based simulation. Contrary to existing methods, our model aims at having a better prediction of the device physical behavior, in particular taking into account contacts with the surrounding blood vessels. Through a Bayesian filter, the predicted shape is corrected with 2D observations of the current real shape, detected and tracked in an image sequence. Such stochastic formulation allows not only to take into account inaccuracies in the navigation model (mechanical characterization of the catheter model, uncertainties on applied constraints, etc), but it also allows to take into account the missing depth information of 2D image features as a further source of uncertainty of the stochastic state.

Given the non-linearity of both the model and the observation processes, we propose to use an Unscented Kalman Filter [15]. One of the major contributions of this work is a solution to the constrained state estimation problem raised by contacts. In stochastics, a constrained estimation occurs when not all the values of the random variable are acceptable samples. In our case, as the device is constrained to stay inside the vessel, the estimated positions cannot assume all the possible values within their probability distribution (e.g. outside the vessel surface). The proposed method casts such constrained estimation as a Non-linear Complementarity Problem (NLCP) solved using a Gauss-Seidel Method.

Several approaches are combined in this work. In this section, we first introduce some generic background about Bayesian filtering. Then, we present the physics based model of the catheter navigation with its dynamics equations. The end of the section describes the whole proposed formalism where both concepts are combined.

2.1 Bayesian Filtering

Bayes filters recursively estimate the probability density function describing the random state of a system. In the discrete domain, such state can be represented as a random variable X_k, with k being the discrete time-step, assumed to evolve according to a process model. The process model can be expressed as a collection of known functions $g_k(\cdot)$ such that:

$$\boldsymbol{X}_k = g_k(\boldsymbol{X}_{k-1}, \nu_k) \tag{1}$$

Other external data may also be available at each time-step providing potentially partial observations $\boldsymbol{Z}_k$ of the current state of the system. Such observations are related to the state through to known observation functions $h_k(\cdot)$:

$$\boldsymbol{Z}_k = h_k(\boldsymbol{X}_k, \omega_k) \tag{2}$$

Both state and observations are affected by random noise processes, respectively ν_k and ω_k. Bayes filters are based on a general prediction-update scheme of the posterior probability $P(\boldsymbol{X}_k|\boldsymbol{Z}_k)$. Given the previous estimation $P(\boldsymbol{X}_{k-1}|\ \boldsymbol{Z}_{k-1})$

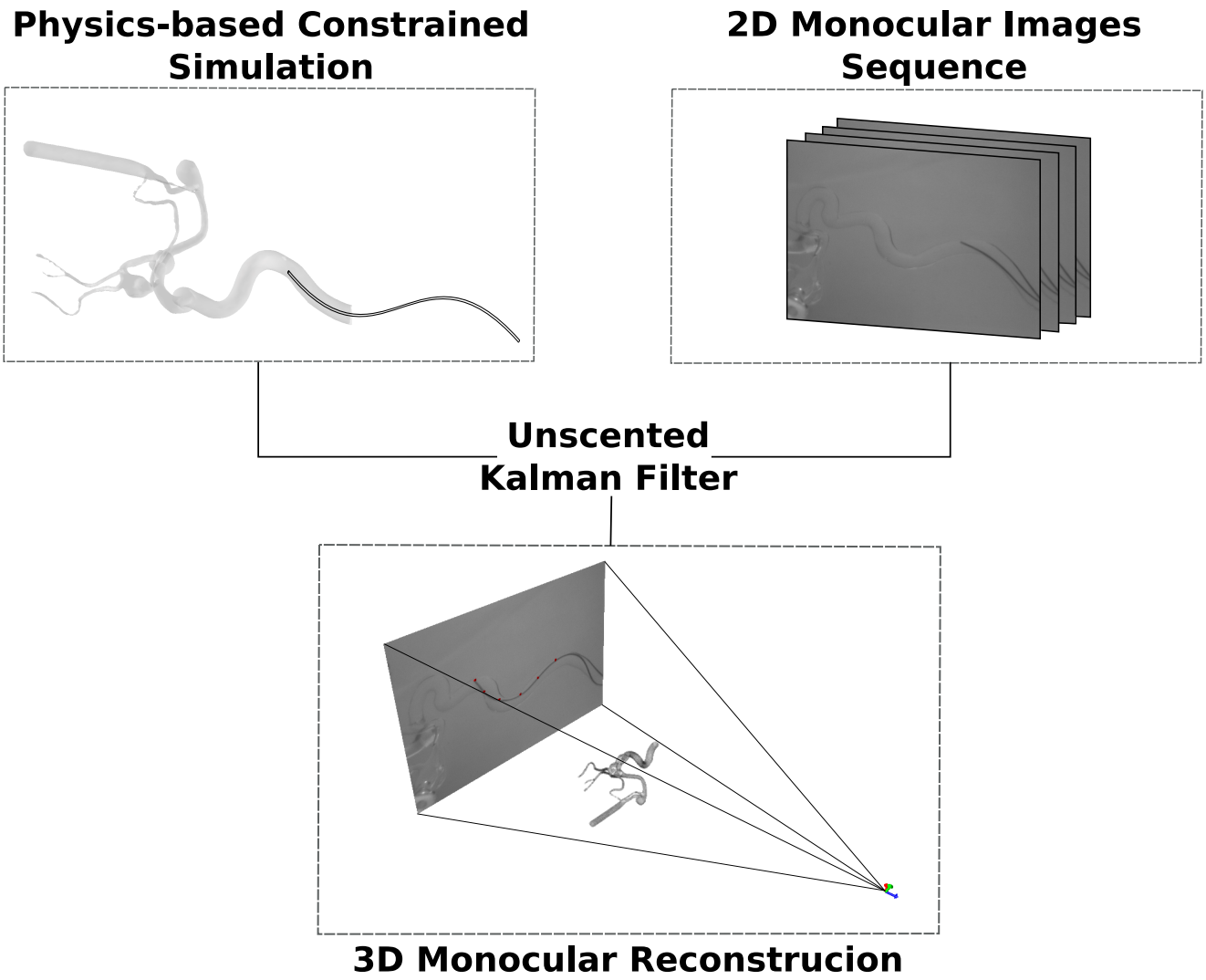

Fig. 2. **Method Overview**. Physics-based constrained simulation provides a model for catheter-like device navigation within blood vessels; 2D monocular images are used to extract information on the current position of the projected device. The 3D shape of the device is recovered by combining them both as respectively the prediction model and the external observations of a Unscented Kalman Filter (UKF).

at time $k-1$, the first step consists of computing a prediction of the probability density function by propagation through the process model g_k: $P(\boldsymbol{X}_k|\boldsymbol{Z}_{k-1})$. Then, the predicted estimate is updated using the current observation, to provide the posterior estimate: $P(\boldsymbol{X}_k|\boldsymbol{Z}_k)$. The final state of the system $\boldsymbol{X}_k$ is thereafter selected according to some optimality criterion (e.g. Maximum A Posteriori or expected value).

Kalman filters [16] are a particular case of Bayes filters where noise processes are assumed to be Gaussian and both process and observation models are linear and can be expressed by matrices $\mathbf{G}_k$ and $\mathbf{H}_k$:

$$\begin{aligned} \boldsymbol{X}_k &= \mathbf{G}_k \boldsymbol{X}_{k-1} + \boldsymbol{\nu}_k, \quad \text{with} \quad \boldsymbol{\nu}_k = \mathcal{N}(0, \boldsymbol{Q}_k) \\ \boldsymbol{Z}_k &= \mathbf{H}_k \boldsymbol{X}_k + \boldsymbol{\omega}_k, \quad \text{with} \quad \boldsymbol{\omega}_k = \mathcal{N}(0, \boldsymbol{R}_k) \end{aligned} \tag{3}$$

Whenever these assumptions are not possible, the Kalman filter formalism may still be used, but some approximations are necessary. For example, the Extended Kalman Filter (EKF) handles non-linear process and observation models, and propagates the system covariance thanks to their first order approximations: $\mathbf{G}_k$ and $\mathbf{H}_k$ are the Jacobian matrices of g_k and h_k [17]. In this work, we decided to use an Unscented Kalman Filter (UKF) [15, 17] that applies a sampling based approach to handle non-linear prediction and observation models (eq.((1)-(2))). The idea behind a UKF is to draw r samples from the current estimate of the posterior probability in such a way that these samples, called *sigma-points*, capture the first two moments of the posterior distribution, with minimum distortion on the third moment [15]. Each sigma-point σ_j is propagated through the non-linear process, then observation models, which enables to compute the transformed mean and covariance of the state. The by-design preservation of the first moments of the probability density function makes UKF a better choice

than EKF when strong non-linearities can be expected. The following table and algorithm summarize the notations used throughout the paper and recall the main steps of a UKF.

Table 1. **Notations : discrete time index k was dropped for simplicity**

$\boldsymbol{X}$ state vector	$\boldsymbol{P}$ model covariance
$\boldsymbol{\sigma}_j$ j^{th} sigma-points	$\mathbf{I}^{(j)}$ unit vector to generate $\boldsymbol{\sigma}_j$
$\boldsymbol{Q}$ model noise covariance matrix	$\boldsymbol{Z}$ observations vector
$\boldsymbol{P}^{\hat{Z}}$ observations covariance	$\boldsymbol{R}$ obs. noise covariance matrix
$\boldsymbol{P}^{\hat{X}\hat{Z}}$ state-observations cross-covariance	$\boldsymbol{K}$ Kalman gain
g prediction function	h observation function

Initialization: set $\boldsymbol{X}_0, \boldsymbol{P}_0, \boldsymbol{Q}_0, \boldsymbol{R}_0$
for *each discrete step* k **do**
  Prediction:
  for $j = 1 : r$ *with* $r =$ *number of sigma-points* **do**
    $\boldsymbol{\sigma}_{j_k} = \boldsymbol{X}_{k-1} + \sqrt{\boldsymbol{P}}_{k-1}\mathbf{I}^{(j)}$ *generate sigma-point*
    $\hat{\boldsymbol{\sigma}}_{j_k} = g_k(\boldsymbol{\sigma}_{j_k}, \boldsymbol{\nu}_k)$ *propagate sigma-point*
  end
  $\hat{\boldsymbol{X}}_k = \mathrm{E}[\hat{\boldsymbol{\sigma}}_k^*]$ *compute predicted state* $\sim$ *sigma-points mean*
  $\hat{\boldsymbol{P}}_k = \mathrm{cov}[\hat{\boldsymbol{\sigma}}_k^*] + \boldsymbol{Q}_k$ *predicted covariance* $\sim$ *sigma-points covariance*
  Correction:
  for $j = 1 : r$ **do**
    $\hat{\boldsymbol{Z}}_{j_k} = h_k(\hat{\boldsymbol{\sigma}}_{j_k})$ *compute predicted observations*
  end
  $\boldsymbol{P}_k^{\hat{X}\hat{Z}} = \mathrm{cov}[\hat{\boldsymbol{\sigma}}_k^*, \hat{\boldsymbol{Z}}^*]$ *compute state-observations cross-covariance*
  $\boldsymbol{P}_k^{\hat{Z}} = \mathrm{cov}[\hat{\boldsymbol{Z}}_k^*, \hat{\boldsymbol{Z}}_k^*] + \boldsymbol{R}_k$ *compute observations covariance*
  $\boldsymbol{K}_k = \boldsymbol{P}_k^{\hat{X}\hat{Z}}(\boldsymbol{P}_k^{\hat{Z}})^{-1}$ *compute Kalman gain*
  $\boldsymbol{X}_k = \hat{\boldsymbol{X}}_k + \boldsymbol{K}_k(\boldsymbol{Z}_k - \mathrm{E}[\hat{\boldsymbol{Z}}_k^*])$ *compute final state*
  $\boldsymbol{P}_k = \hat{\boldsymbol{P}}_k - \boldsymbol{P}_k^{\hat{X}\hat{Z}}(\boldsymbol{P}_k^{\hat{Z}})^{-1}(\boldsymbol{P}_k^{\hat{X}\hat{Z}})^t$ *compute final covariance*
end

Algorithm 1: Unscented Kalman Filter algorithm. See Table 1 for notations. The symbol * stands for the whole set of sigma-points, whereas the subscript j indicates a single sample.

2.2 Catheter Navigation Model

Devices such as catheters or guidewires are flexible but inextensible non-linear elastic objects. In this paper, we use a physics-based model based on beam theory [18], solved using an efficient co-rotational finite element (FE) approach [19]. Our model is represented as a series of N serially-linked beam elements, where each node has 6 Degrees of Freedom (DoFs) [20] (see Fig. 3.a). To simulate the navigation of the device inside the anatomy, we suppose each node of the model to be subjected to an external force (see Fig. 3.b), which allows its insertion within the blood vessel, while being constrained inside the surface (obtained from segmentation of pre-operative images).

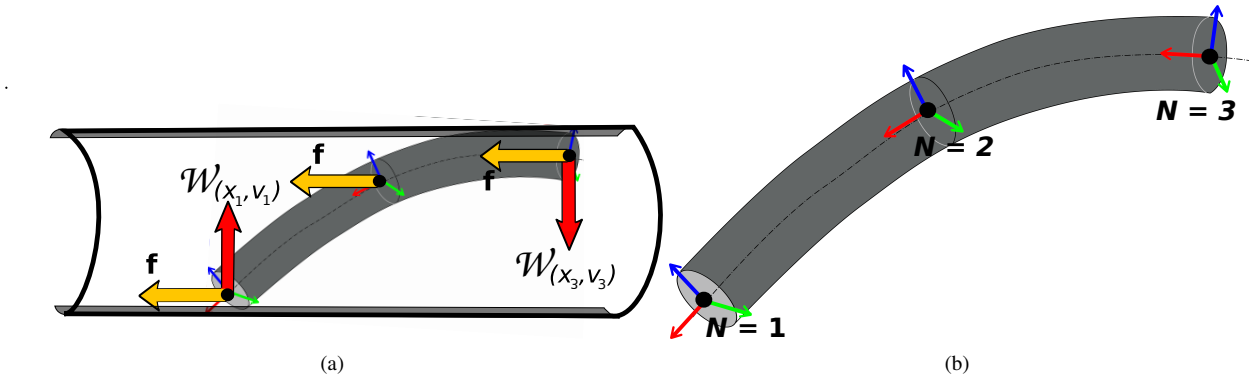

(a) (b)

Fig. 3. **FE Physics-Based Model**. (a) Lateral view of the simulated device inside the surface. Yellow arrows represent insertion forces $\mathbf{f}$ on each node, used to produce catheter forward motion; red arrows are the surface constraint forces $\mathcal{W}(\mathbf{x}_i, \mathbf{v}_i)$ applied on the i^{th} node whenever a contact occurs. (b) The device is modeled as a series of N connected 6 DoFs beams

2.2.1 Free motion dynamics

The dynamics of the interventional device (not subjected to any external constraints) is governed by Newton's second law of motion, here expressed as second order differential equation:

$$\mathbf{M}\ddot{\mathbf{x}} = f(\mathbf{x}, \dot{\mathbf{x}}) \tag{4}$$

where generally speaking $\mathbf{M}$ is the mass, $f(\cdot)$ the applied forces, and $(\mathbf{x}, \dot{\mathbf{x}}, \ddot{\mathbf{x}})$ express respectively position, velocity and acceleration of a catheter's node. Since we model deformable bodies which may undergo stiff constraints, an Implicit Integration approach is more appropriate. In addition, an implicit integration scheme using large time steps, requires less computational time compared to explicit methods, making it more convenient for real-time applications. We chose a Backward Euler method, which imposes to rewrite eq.((4)) as a first-order differential equation:

$$\frac{d}{dt}\begin{pmatrix}\mathbf{x}\\ \dot{\mathbf{x}}\end{pmatrix} = \begin{pmatrix}\dot{\mathbf{x}}\\ \mathbf{M}^{-1}f(\mathbf{x}, \dot{\mathbf{x}})\end{pmatrix} \tag{5}$$

Collisions between objects usually lead to discontinuity in the velocities. To handle non-smooth dynamics while enabling fast computations, we use a *time-stepping* method [21]. The discrete variables are then expressed as $\mathbf{x} = \mathbf{x}(t)$, $\mathbf{v} = \dot{\mathbf{x}}(t)$ with the respective differences $\mathbf{\Delta x} = \mathbf{x}(t+T) - \mathbf{x}(t)$ and $\mathbf{\Delta v} = \mathbf{v}(t+T)$ - $\mathbf{v}(t)$ (T is the time-step). Eq.((5)) expressed in the discrete domain, becomes:

$$\begin{pmatrix}\mathbf{\Delta x}\\ \mathbf{\Delta v}\end{pmatrix} = T\begin{pmatrix}\mathbf{v} + \mathbf{\Delta v}\\ \mathbf{M}^{-1}f(\mathbf{x} + \mathbf{\Delta x}, \mathbf{v} + \mathbf{\Delta v})\end{pmatrix} \tag{6}$$

This equation is then linearized using a first order Taylor series expansion of the term $f(\mathbf{x} + \mathbf{\Delta x}, \mathbf{v} + \mathbf{\Delta v})$:

$$f(\mathbf{x} + \mathbf{\Delta x}, \mathbf{v} + \mathbf{\Delta v}) \sim \mathbf{f} + \frac{\partial f}{\partial \mathbf{x}}\mathbf{\Delta x} + \frac{\partial f}{\partial \mathbf{v}}\mathbf{\Delta v} \tag{7}$$

Such linearization corresponds to the first iteration of the Newton-Raphson algorithm. Limited Newton-Raphson iterations enable faster computations, with the risk of not obtaining full convergence of the solution. In our scenario, given the hypothesis of small displacements, a single iteration is usually sufficient to provide a reliable solution. The implicit velocity update is then computed as:

$$(\mathbf{M} - T\frac{\partial f}{\partial \mathbf{v}} - T^2\frac{\partial f}{\partial \mathbf{x}})\mathbf{\Delta v} = T(\mathbf{f} + T\frac{\partial f}{\partial \mathbf{x}}\mathbf{v}) \tag{8}$$

The partial derivatives of elastic forces can be defined as $\mathbf{K} = \frac{\partial f}{\partial \mathbf{x}}$ and $\mathbf{B} = \frac{\partial f}{\partial \mathbf{v}}$, respectively the stiffness and damping matrix of our system. Eq. (8) rewrites as a linear system:

$$\underbrace{(\mathbf{M} - T\mathbf{B} - T^2\mathbf{K})}_{\mathbf{A}} \boldsymbol{\Delta}\mathbf{v} = \underbrace{T(\mathbf{f} + T\mathbf{K}\mathbf{v})}_{\mathbf{b}} \tag{9}$$

The solution $\boldsymbol{\Delta}\mathbf{v}$ provides the variation of velocity which is then integrated to compute the state of our system at the next time step:

$$\begin{aligned} \mathbf{v}_{(t+T)} &= \mathbf{v}_t + \boldsymbol{\Delta}\mathbf{v} \\ \mathbf{x}_{(t+T)} &= \mathbf{x}_t + T\mathbf{v}_{(t+T)} \end{aligned} \tag{10}$$

Equations ((9)-(10)) define the *free-motion* of the object, describing its dynamic behavior when subject to internal and external forces.

2.2.2 Contact Constraints

The interventional device is forced to remain within the blood vessels through boundary constraints expressed as non-linear inequalities. Such contact constraints are applied through Lagrange multipliers in a prediction-correction approach: first a free motion is performed (prediction) and then contact forces are applied to all positions violating the boundary constraints (correction). During the first step, potential contact points are identified through a proximity detection between catheter nodes and the vessel partitioned surface (for details see [22, 23]). For each node of the catheter, the closest point on the surface is determined, with $\mathbf{n}$ the normal to the surface at that point. The collision response for each node is then performed based on Signorini's law:

$$\begin{cases} \boldsymbol{\delta}_\mathbf{n} \geq 0 \\ \boldsymbol{\lambda}_\mathbf{n} \geq 0 \\ \boldsymbol{\delta}_\mathbf{n} \cdot \boldsymbol{\lambda}_\mathbf{n} = 0 \end{cases} \tag{11}$$

where $\delta_\mathbf{n}$ represents the interpenetration which must be ensured non negative and $\boldsymbol{\lambda}_\mathbf{n}$ is the contact force applied to correct potential violation of the constraint (for details see [23]). Friction phenomena are taken into account according to Coulomb's friction law. A component of the contact forces will hence depend on a friction parameter μ:

$$\boldsymbol{\lambda}_\mathbf{T} = -\mu ||\boldsymbol{\lambda}_\mathbf{n}|| \frac{\delta_\mathbf{T}}{||\delta_\mathbf{T}||} \tag{12}$$

From a mathematical point of view, such interactions can be expressed by a non-linear function $\mathcal{W}(\mathbf{x}, \mathbf{v})$ depending on the positions of both objects in contact. Given the linearized problem, the transpose of the Jacobian $\mathbf{J} = \frac{\partial \mathcal{W}}{\partial \mathbf{x}}$ expresses the directions along which all the contact forces $\boldsymbol{\lambda}$, for all points in contact, are applied. Hence equation ((9)), taking into account inequality constraints, becomes:

$$\begin{cases} \mathbf{A}\boldsymbol{\Delta}\mathbf{v} = \mathbf{b} + \mathbf{J}^T\boldsymbol{\lambda} \\ \mathbf{J}^T\boldsymbol{\Delta}\mathbf{v} = \boldsymbol{\delta} \end{cases} \tag{13}$$

The above system provides a NLCP (Non-linear Complementarity Problem) that is solved using a Gauss-Seidel Method ([23]).

2.2.3 Model parameterization

The physics-based model presented above can represent the shape and dynamics of a catheter or guidewire under complex shape constraints due to the vascular anatomy. However, to exactly match the behavior of a real device, this model needs to be parameterized. The parameters which are known to influence the simulation are: 1) intrinsic parameters such as the mass, stiffness and radius of the device, which appear in matrices $\mathbf{M}, \mathbf{B}, \mathbf{K}$ of Eq. (9)); and extrinsic parameters such as contact forces or drag forces due to blood flow which appear on the right hand side of Eq. 4.

In our context, we assume that mechanical parameters ($\mathbf{M}$, $\mathbf{B}$, $\mathbf{K}$) can be determined either from literature or through simple measurements. On the other hand, forces applied to the device are more difficult to estimate, and are likely to vary along the path of the device. To illustrate this point, let us take a more detailed look at the influence of the friction coefficient μ which appears in Eq. 9. Contrary to other parameters, the friction coefficient is dependent on several factors, such as patient anatomy, type of catheter, blood flow, etc. and cannot be known accurately. Fig. 4 actually shows that even small variations in the friction coefficient μ may lead to very different results. In this experiment, each simulation used a different value of μ within the interval $[0; 0.08]$. Such small values correspond to no or limited friction, as it is the case in healthy vessels. We can see that the difference between all possible configurations increases through time, due to the cumulative effect of the friction.

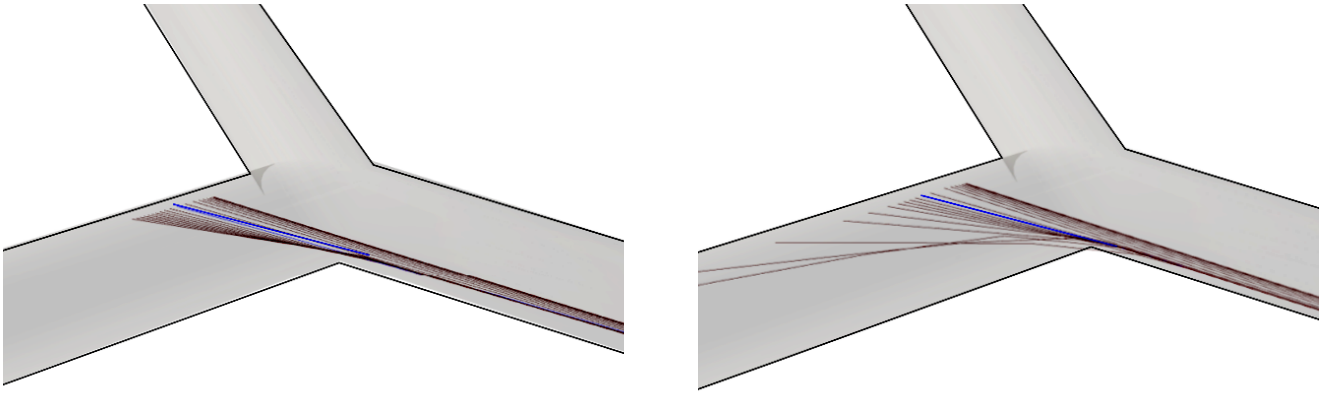

Fig. 4. **Friction Coefficient Effect**. Comparison of catheter shapes simulated with different values of the friction coefficient μ (left: early simulation time, right: late simulation time). The ground-truth value is $\mu_{GT} = 0.04$ (blue shape). The other red shapes were obtained by sampling μ in $[0, 0.08]$ every 0.004 (lowest values are on the left of the blue shape in each view). Friction is a cumulative phenomenon, which explains why even small deviations from the real value can generate very different behaviors over time.

Such errors in the simulation (due to parameter uncertainty) can, however, be compensated through information extracted from the image. In the next sections, we will show how 2D observations can be enough to balance the limited inaccuracy of the model.

2.3 Image Feature Observations

The projected shape of the catheter should be detected in fluoroscopic images. Several solutions have been proposed to detect and track a curve in an image sequence [24, 25, 26]. We made the assumption extensively used in monocular reconstruction to detect and track 2D features corresponding to known 3D points. In practice, the catheter is assumed to be tagged with M radio-opaque markers $\{P_i = (x_i, y_i, z_i)\}_{i\in[1,M]}$, equally distributed along the catheter length. Each marker P_i is thus related to the catheter nodes through a constant linear mapping $\mathcal{M}_i$ (see Fig. 5). In the image, each marker is detected at pixel coordinates $q_i = (u_i, v_i)$ which are related to the 3D marker coordinates through the $[3 \times 4]$ projection matrix $\mathbf{C}$, such that

$$\underline{\mathrm{q}}_i = \mathbf{C}\,\underline{\mathrm{P}}_i \tag{14}$$

where the underline notation expresses homogeneous coordinates. $\mathbf{C}$ only depends on the X-ray view incidence, which is assumed constant during the acquisition of a fluoroscopic sequence. This matrix can be accurately estimated from the view parameters (angles, source-to-image distance, ...) with a calibrated vascular C-arm [27]. We assume 2D-3D correspondences, between detected image-features and the FE model, to be known.

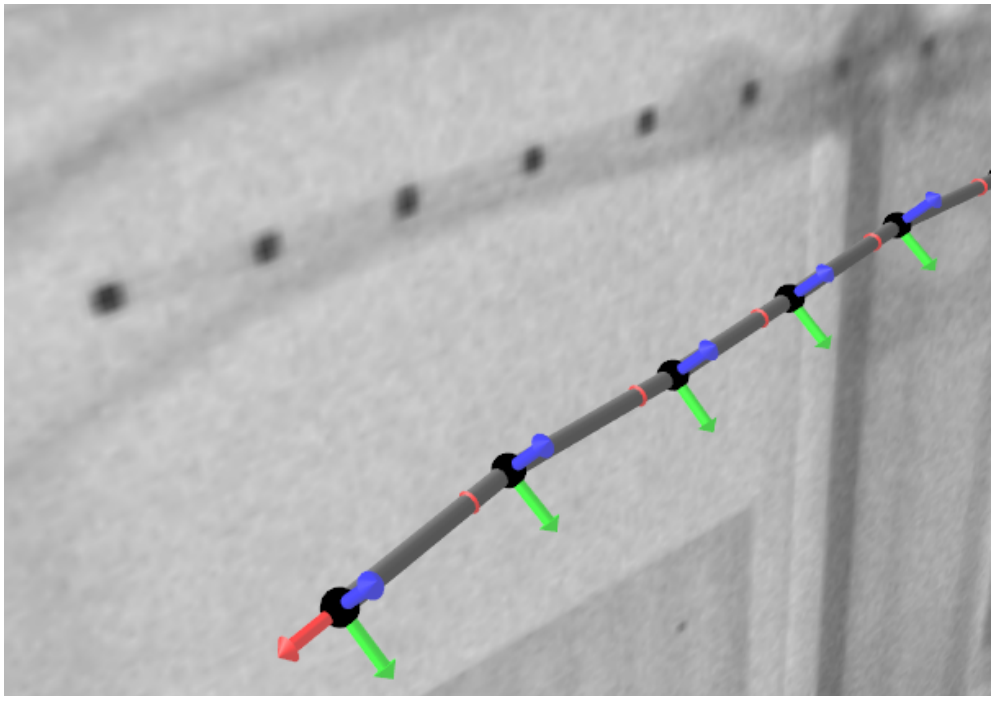

Fig. 5. **Image Feature Detection**. Radio-opaque markers are related to 6 DoF catheter's nodes through a known constant mapping $\{P_i = \mathcal{M}_i(\mathbf{x})\}$. Without loss of generality, we suppose markers to exactly match the nodes.

2.4 Combined Framework

The physics-based simulation presented in sec. 2.2 provides a prediction of the 3D shape of the device within blood vessels. Due to model uncertainties, sec. 2.2.3, the predicted shape does not perfectly correspond to the reality. 2D fluoroscopic image features (Sec. 2.3) give partial information on the current state of the catheter, and may be used to correct the prediction provided by the simulation. We propose to combine the physics-based model with external 2D observations through a Bayesian filter. The use of the filter allows to retrieve an accurate 3D shape taking into account the uncertainty on both the model and the external measurements, while dealing with observations acquired from ambiguous angle of view, and handling complex behaviors related to contacts and friction phenomena. In the following notation, the index i specifies the catheters nodes, k indicates the discrete time-step, and j refers to sigma-points.

2.4.1 State Vector

Usually, in Kalman Filter for trajectory estimation, the state vector is composed of position, velocity and acceleration of the object. In our case, we estimate the positions and velocities of each catheter node given that, using the time integration scheme presented in Eq. (5), the acceleration is in fact expressed as a difference of velocities. Considering the i^{th} node, the state vector can hence be expressed as:

$$\boldsymbol{X}(i) = [\underbrace{x_i, y_i, z_i, \psi_i, \theta_i, \phi_i}_{\textbf{position } \mathbf{x}_i^t}, \underbrace{v_{x_i}, v_{y_i}, v_{z_i}, v_{\psi_i}, v_{\theta_i}, v_{\phi_i}}_{\textbf{velocity } \mathbf{v}_i^t}] \tag{15}$$

with $i \in (1, N)$ and N being the number of serially linked beams. Given that position and velocity are expressed taking into account 6DoFs, the whole state will be $\boldsymbol{X} \in \mathbb{R}^{12N}$.

2.4.2 Prediction Model

The temporal evolution of the state results from a two step process: first solve Eq. (13) for $\boldsymbol{\Delta}\mathbf{v}$ and then update the positions $\mathbf{x}$ and velocities $\mathbf{v}$ through Eq. (10).

The noise on this process mainly comes from an uncertain characterization of the FE model, that it is propagated to the estimated $\boldsymbol{\Delta}\mathbf{v}$, solution of Eq. (13). The resultant noise is modeled as a Gaussian additive random term ν_k. As a result, our

process model is given by

$$\mathbf{A}_k \boldsymbol{\Delta}\mathbf{v}_k = \mathbf{b}_k + \mathbf{J}_k^T \boldsymbol{\lambda}_k \tag{16}$$

$$\mathbf{J}_k^T \boldsymbol{\Delta}\mathbf{v}_k = \boldsymbol{\delta}_k \tag{17}$$

$$\mathbf{v}_k = \mathbf{v}_{k-1} + (\boldsymbol{\Delta}\mathbf{v}_k + \nu_k) \tag{18}$$

$$\mathbf{x}_k = \mathbf{x}_{k-1} + T\mathbf{v}_k \tag{19}$$

Eqs. (16) and (17) provide $\boldsymbol{\Delta}\mathbf{v}_k$, that is tainted with random noise ν_k, which affects the velocities $\mathbf{v}_k$ (Eq. (18)) and positions $\mathbf{x}_k$ (Eq.(19)). We assume an independent and constant noise so that $E[\nu_k(\nu_k)^t] = \sigma_{mod}\mathbf{I}_{6N}$.

This results in the state covariance matrix expressed as:

$$\boldsymbol{Q} = \mathbf{I}_N \otimes \begin{pmatrix} \mathbf{0}_{6\times6} & \mathbf{0}_{6\times6} \\ \mathbf{0}_{6\times6} & \sigma_{mod}^2\mathbf{I}_6 \end{pmatrix} \tag{20}$$

where $\otimes$ is the Kronecker product and $\mathbf{I}_N$ is the $N \times N$ identity matrix.

2.4.3 Observation Model

Observations are the projection of the radio-opaque markers, detected in the images:

$$\boldsymbol{Z}(i) = q_i = [u_i, v_i]^t \qquad \forall i \in [1, M] \tag{21}$$

According to our observation model, the i^{th} detected feature will depend on the corresponding 3D marker, through the calibrated projection matrix:

$$\underline{\boldsymbol{Z}}(i) = \mathbf{C}\,[x_i, y_i, z_i, 1]^t = \begin{pmatrix}\mathbf{U}\ \mathbf{0}_{3\times9}\ \mathbf{V}\end{pmatrix} \begin{bmatrix}\mathbf{X}(i) \\ 1\end{bmatrix} = \mathbf{C}_+\,\underline{\mathbf{X}}(i) \tag{22}$$

where $\mathbf{U}$ and $\mathbf{V}$ are respectively a 3×3 matrix and a 3-vector such that $\mathbf{C} = (\mathbf{U}\,\mathbf{V})$. The observation function $h_k(\cdot)$ is therefore constant : $h_k = h$. For the sake of simplicity, we assumed here that identity mappings relate markers to nodes such that a node is defined at each marker location, such that M, the number of markers, equals N, the number of nodes.

The observation vector $\boldsymbol{Z}_k \in \mathbb{R}^{2N}$ concatenates the locations of all the 2D markers detected in the image at time k. We assume that all observations are independent and that the noise ω on the observations does not depend on the acquisition time. Therefore, its covariance matrix is constant and diagonal: $\boldsymbol{R} = \sigma_{obs}^2\mathbf{I}_{2N}$.

2.4.4 Filter Workflow and Computation Time

The *simplex method* [28] was used to generate the r sigma-points with a minimum computation cost: it requires only $r = p + 1$ sigma-points, where $p = 12N$ is the state vector size. A generic sigma-points is expressed as

$$\boldsymbol{\sigma}_j = [\boldsymbol{\sigma}_{\mathbf{x}_1}, \boldsymbol{\sigma}_{\mathbf{v}_1}, \cdots, \boldsymbol{\sigma}_{\mathbf{x}_N}, \boldsymbol{\sigma}_{\mathbf{v}_N}]_j^t \quad \text{with } j \in (1, r) \tag{23}$$

Alg.(2) summarizes an UKF estimation, modified to take into account our specific process and observation model. Fig. 6 summarizes the global pipeline in which filter and simulation are combined. In the prediction phase, an entire simulation step is run for every sigma-point $\boldsymbol{\sigma}_j$. From each propagated $\hat{\boldsymbol{\sigma}_j}$ we can compute the predicted observations $\hat{\boldsymbol{Z}}_j$, through the observation function $h(\cdot)$. A major challenge of our method lies in achieving high computation time. Whereas a classic physics-based constrained simulation may be performed in real-time (over 25 FPS), such combined approach entails higher computation times due to the multiple simulations performed during each time-step. In order to optimize computation time, one possible solution is to reduce the state vector size by not taking into account all the degrees of freedom of the mechanical model. Results reported in Section 3.5 were obtained with a reduced state vector where the orientations were removed: $\boldsymbol{X}(i) = [x_i, y_i, z_i, v_{x_i}, v_{y_i}, v_{z_i}, v_{\psi_i}, v_{\theta_i}, v_{\phi_i}]$. In the process, the orientations $(\psi_i, \theta_i, \phi_i)$ were mathematically computed from the estimated positions (x_i, y_i, z_i).

Initialization: set $\boldsymbol{X}_0, \boldsymbol{P}_0, \boldsymbol{Q}, \boldsymbol{R}$
for *each simulation step* k **do**
  Prediction:
  for $j = 1 : r$ *with* $r =$ *number of sigma-points* **do**
    generate sigma-points
    $[\boldsymbol{\sigma}_{\mathbf{x}}, \boldsymbol{\sigma}_{\mathbf{v}}]_{j_k} = [\mathbf{x}_{k-1}, \mathbf{v}_{k-1}] + \sqrt{\boldsymbol{P}}_{k-1}\mathbf{I}^{(j)}$
    propagate sigma-points (eqs. (16)- (19)*)*
    $\mathbf{A}\boldsymbol{\Delta\sigma}_{\mathbf{v}_{j_k}} = \mathbf{b} + \mathbf{J}^T\boldsymbol{\lambda}$
    $\mathbf{J}^T\boldsymbol{\Delta\sigma}_{\mathbf{v}_{j_k}} = \boldsymbol{\delta}$
    $\hat{\boldsymbol{\sigma}}_{\mathbf{v}_{j_k}} = \boldsymbol{\sigma}_{\mathbf{v}_{j\ k-1}} + \boldsymbol{\Delta\sigma}_{\mathbf{v}_{j_k}}$
    $\hat{\boldsymbol{\sigma}}_{\mathbf{x}_{j_k}} = \boldsymbol{\sigma}_{\mathbf{x}_{j\ k-1}} + T\hat{\boldsymbol{\sigma}}_{\mathbf{v}_{j_k}}$
  end
  $\hat{\boldsymbol{X}}_k = \mathrm{E}[\hat{\boldsymbol{\sigma}}_k^*]$
  $\hat{\boldsymbol{P}}_k = \mathrm{cov}[\hat{\boldsymbol{\sigma}}_k^*] + \boldsymbol{Q}$;
  Correction:
  for $j = 1 : r$ **do**
    $\underline{\hat{\boldsymbol{Z}}}_{j_k} = \mathbf{C}_+\,\underline{\hat{\boldsymbol{\sigma}}}_{j_k}$ *see eq.* (22)
  end
  $\boldsymbol{P}_k^{\hat{X}\hat{Z}} = \mathrm{cov}[\hat{\boldsymbol{\sigma}}_k^*, \hat{\boldsymbol{Z}}_k^*]$
  $\boldsymbol{P}_k^{\hat{Z}} = \mathrm{cov}[\hat{\boldsymbol{Z}}_k^*, \hat{\boldsymbol{Z}}_k^*] + \boldsymbol{R}$
  $\boldsymbol{K}_k = \boldsymbol{P}_k^{\hat{X}\hat{Z}}(\boldsymbol{P}_k^{\hat{Z}})^{-1}$
  $\boldsymbol{X}_k = \hat{\boldsymbol{X}}_k + \boldsymbol{K}_k(\boldsymbol{Z}_k - \mathrm{E}[\hat{\boldsymbol{Z}}_k^*])$
  $\boldsymbol{P}_k = \hat{\boldsymbol{P}}_k - \boldsymbol{P}_k^{\hat{X}\hat{Z}}(\boldsymbol{P}_k^{\hat{Z}})^{-1}(\boldsymbol{P}_k^{\hat{X}\hat{Z}})^t$
end

Algorithm 2: UKF for physics-based constrained simulation. Index i is omitted in the notation.

2.4.5 Constrained State Estimation

The catheter bounded within the vessel surface represents, from the filter point of view, a problem known as Constrained State Estimation [29]. During the prediction phase, random sampling of the Gaussian distribution may generate some sigma-points $\boldsymbol{\sigma}_j$ whose positions fall outside the vessel surface (Fig. 7(b)), representing configurations not physically coherent. From the simulation point of view, such scenario corresponds to a configuration of the catheter not respecting the constraint ($\boldsymbol{\delta}_{\mathbf{n}} \leq 0$). The collision response model presented in Sec. 2.2.2 enables to solve this problem. During the propagation step, nodes detected as crossing the vessel wall are corrected through contact forces, and projected back into the space of physically acceptable states (i.e. with positions inside the vessel) (see Fig.7). Furthermore, non-linear interactions with the surrounding surface, taking into account non-sliding contacts (see Eq. (12)), enables to further improve the prediction of the catheter shape. The proposed Bayesian filter process enables the fusion of mechanical constraints with the geometric constraints provided by 2D image features. The number of possible solutions to the ill-posed 2D-3D reconstruction problem is thereby reduced down to a single high probability, and correct, hypothesis in the vast majority of cases. Experiments reported in the next section will back up this assertion. As stated in sec.2.2.3, the mechanical characterization of the catheter is assumed to be known and applied constraints are identified as the main source of model noise. We conducted a one-at-a-time sensitivity analysis on the mechanical parameters implied in constraints expression, using a Y-shaped bifurcation synthetic model (see also Sec. 3.2). The friction coefficient μ stood out as the major impacting factor on the simulated catheter shape (as shown in Fig. 4).

3 Experimental Set-Up and Results

3.1 Overview and error metrics

We tested the method to retrieve the 3D shape of a navigating device from 2D images, both in a synthetic environment and in the real world. In both cases, a ground truth 3D shape was available to compare our result with. Tests have been carried out to estimate the sensitivity of the filter to model uncertainty, observation noise and parameters tuning. In particular, our validation aims at demonstrating how our approach can naturally handle uncertainties related to complex dynamics, such as collision and friction phenomena, as well as observation uncertainties due to ambiguous acquisition views.

The reconstructed 3D shape of the catheter was compared with the known ground-truth, using the 3D Hausdorff distance, the Euclidean distance between tip points and the mean distance on the 1 cm distal segment (closest to tip) of the catheter. These metrics have been evaluated using a B-spline interpolation to resample the 3D shapes (100 points along the catheter

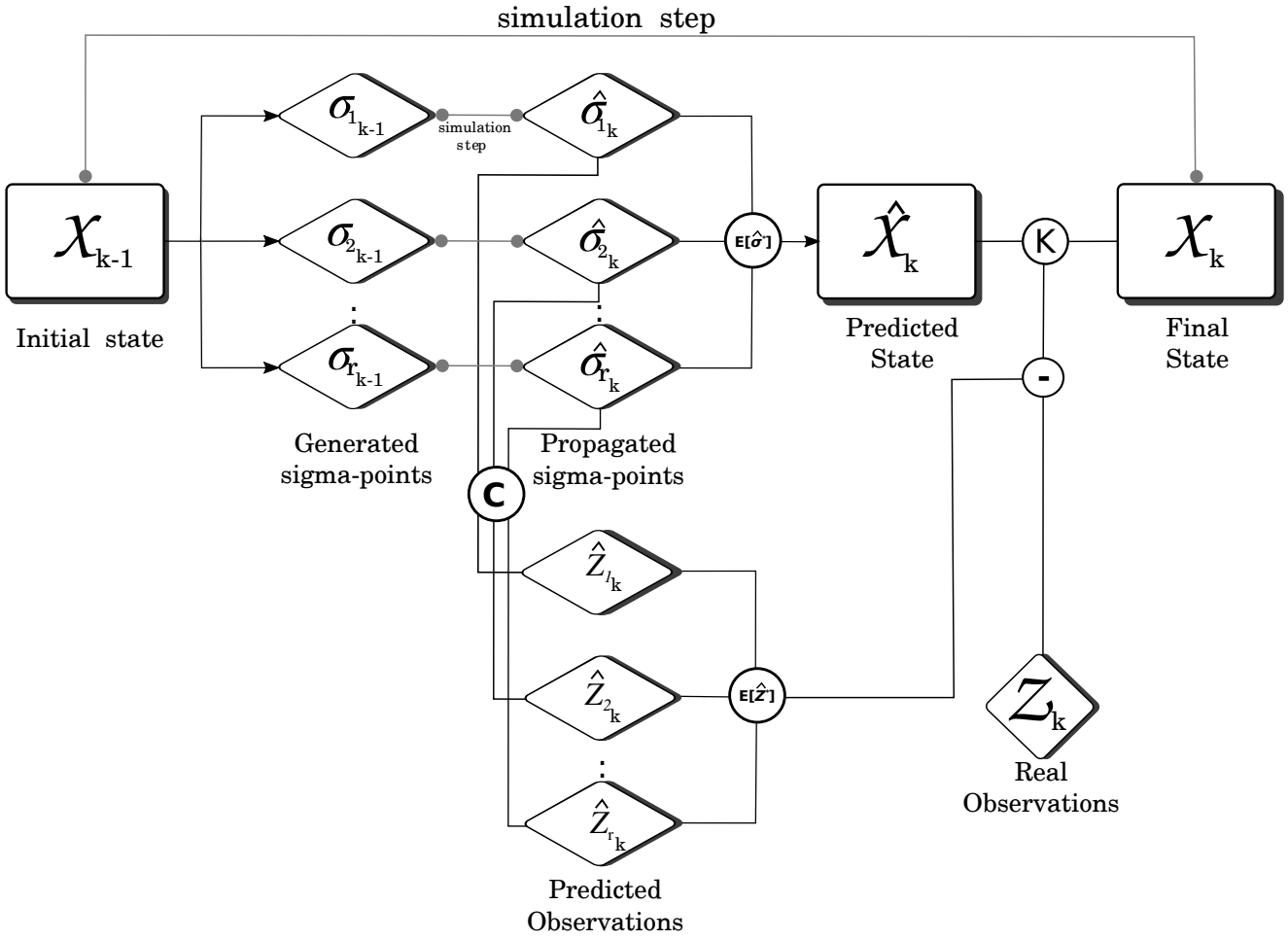

Fig. 6. **Computation Overview**. One single simulation-step is composed of several filter-steps. Filter final state will provide the mechanical state of the catheter to be used in the following simulation step.

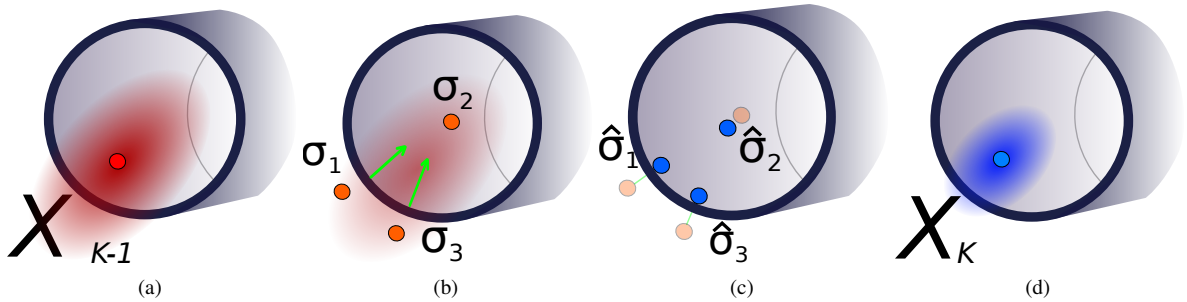

Fig. 7. **Constrained State Estimation**.(a) Red dot represents a catheter node, described with a certain covariance. Blue segments represent the surface where red normals point to the inside. (b) Generated sigma-points may fall outside the geometry. Their position is then corrected during propagation (c) through collision response, since they are interpenetrated objects. (d) Predicted mean and covariance are hence computed from propagated samples.

shape). We focused on the tip and distal segment of the device, because it is the part most subject to variations during the insertion and of the highest importance for clinicians.

3.2 Synthetic Validation

The synthetic setup provided a fully controlled ground truth and allowed to evaluate the robustness of the method to inaccuracies in the process model and to filter parameters tuning.

3.2.1 Ground Truth Reference

A Y-shaped surface, mimicking a vessel bifurcation, was generated by connecting 3 cylinders of 1 cm in diameter. The deterministic model of physics-based constrained-based simulation (Sec. 2.2) was used to simulate a 10 cm long catheter, modeled as a series of 9 connected beams ($N = 10$ nodes). The mechanical parameters of the FE model were chosen according to manufacturers data for devices currently used in clinical practice; the insertion force was initialized according to a desired displacement, and the friction coefficient describing contacts, eq. 12, was set according to literature [30]. All the parameters are summarized in table Tab. 2. The catheter navigation in the Y-shaped vessels was simulated during 2000 time steps, corresponding to a full insertion of the catheter in the blood vessel.

Table 2. **Ground truth Simulation Parameters**

Young Modulus	$\mathbf{E}_{GT}$	1e6	*[Pa]*
Radius	$\mathbf{r}_{GT}$	0.4	*[mm]*
Mass	$\mathbf{m}_{GT}$	0.5	*[g]*
Insertion Force	$\mathbf{f}_{GT}$	0.5e-3	*[N·**T**]*
Friction Coefficient	$\boldsymbol{\mu}_{GT}$	0.04	
time-step	$\mathbf{T}$	0.001	

3.2.2 2D Observations

2D image-features were generated by projecting the ground truth positions under two different view incidences (see Fig. 8): one from the side were the view of the bifurcation is ambiguous (a catheter viewed in the vessels could be in any bifurcating branch), and one from the top with a clear view of the bifurcation. At each time step of the simulated insertion, an X-ray like image of the scene was rendered for each view, using a graphical model of the catheter equipped with markers. The 2D image features were thereafter automatically detected in these images, 3 different instances of random Gaussian noise was added to their locations. A standard deviation of 0.1 pixels was chosen to be consistent with the level of detection error encountered in actual images. Thereby, 6 different data-sets of 2D observations were generated.

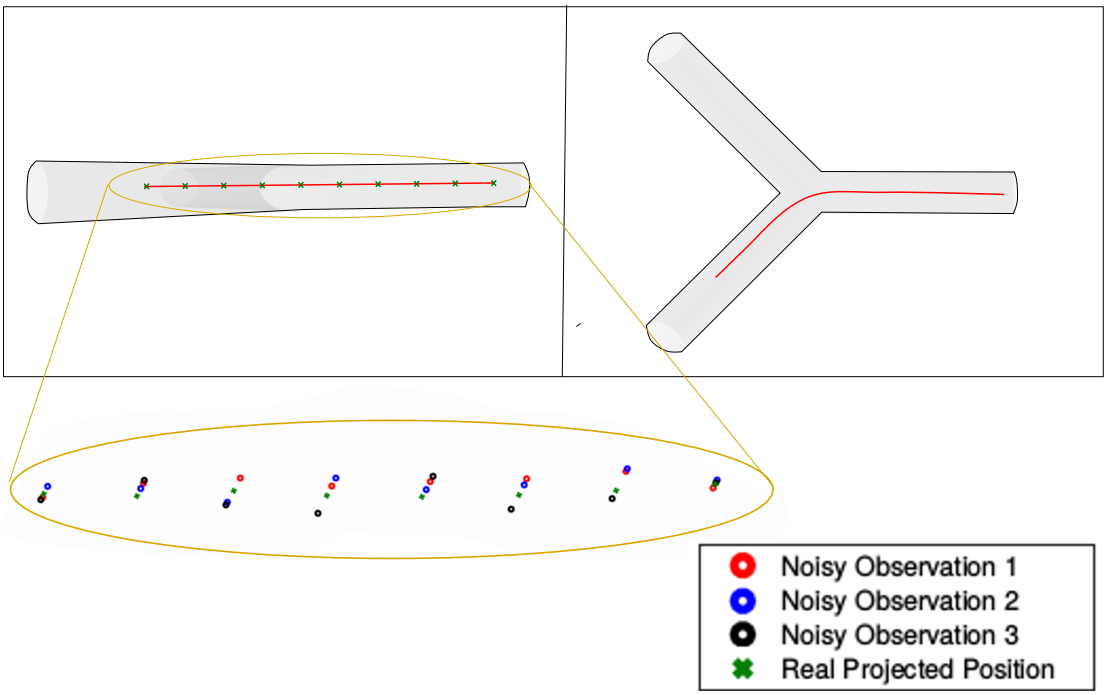

Fig. 8. **Observations**. Two different views for 2D observations, side and top views. 2D observations were created by rendering the virtual catheter, equipped with markers, in each view, detecting the markers, and adding a Gaussian noise to their locations. Three instances of noisy observations were created for each view.

3.2.3 Stochastic Environment: Process Model

Inaccuracies in the prediction by simulation are due do uncertainties on the FE model parameterization. In particular, as stated above, the friction coefficient μ is the major impacting factor in the case of simulation constrained due to collisions. In order to evaluate the impact of the misknowledge we will have in practice on such parameterization, we tested our filter with 20 different process model configurations, each corresponding to a different value for μ, ranging from 0 (i.e. no friction) to 0.08 (i.e. twice the ground truth value, and excluding the ground truth value 0.04) by steps of 0.004 (see Fig. 4). It is noteworthy that usual acceptable uncertainty lies in a range of 10-20%, but we wanted to test the filter capacity to deal with larger errors. Other parameters were the same as the reference model (Tab. 2).

3.2.4 Stochastic Environment: Filter Parameters Tuning

Filters parameters consist in $\boldsymbol{P}_0$, the initial state covariance, $\boldsymbol{Q}$, the process noise covariance and $\boldsymbol{R}$, the observation noise covariance. Such parameters should be initialized to fit the actual level of noise tainting both the process and the observations, which is usually very difficult to set in practice. In our synthetic, fully controlled, environment, though, these parameters are either known ($\boldsymbol{R}$) or can be evaluated ($\boldsymbol{P}_0$ and $\boldsymbol{Q}$). A full state vector was used here (12 values per node).

The observation noise covariance was set to 0.1 pixels. For the latter case, variations on the state emanate here from the error on the friction coefficient. We estimated the state covariance following a Monte Carlo approach based on the 20 process configurations described above. The statistics on the positions and velocities were only computed on the distal segment of the catheter. This led us to set the state covariance matrix to

$$\boldsymbol{P}_0 = \mathbf{I}_N \otimes \begin{pmatrix} \sigma^2_{\mathbf{x}_{mod}}\mathbf{I}_6 & \mathbf{0}_{6\times 6} \\ \mathbf{0}_{6\times 6} & \sigma^2_{\mathbf{v}_{mod}}\mathbf{I}_6 \end{pmatrix} \tag{24}$$

with $\sigma_{\mathbf{x}_{mod}} = [10^{-3}\text{ m}, 10^{-5}\text{ rad}]$ and $\sigma_{\mathbf{v}_{mod}} = [10^{-2}\text{ m/s}, 10^{-3}\text{ rad/s}]$. Similarly, $\boldsymbol{Q}$ was initialized with $\sigma_{mod} = \sigma_{\mathbf{v}_{mod}}$ (see Eq. 20).

To evaluate our filter performance against its parameterization, we ran it with 3 different model configurations: the nominal configuration $\mathcal{P} = [\boldsymbol{P}_0, \boldsymbol{Q}]$ as measured above, an overestimation $\mathcal{P}_{sup} = 1.75^2\mathcal{P}$ where standard deviations are multiplied by 1.75 and an underestimation $\mathcal{P}_{inf} = 0.25^2\mathcal{P}$. Besides, two noise covariance values were also considered: the nominal $\boldsymbol{R}_1$ with an observation noise of 0.1 pixels and $\boldsymbol{R}_2$ with an observation noise of 0.01 pixels.

As a consequence, the filter was ran with 6 different parameterizations: $[\mathcal{P}, \boldsymbol{R}_1]$, $[\mathcal{P}, \boldsymbol{R}_2]$, $[\mathcal{P}_{sup}, \boldsymbol{R}_1]$,$[\mathcal{P}_{sup}, \boldsymbol{R}_2]$, $[\mathcal{P}_{inf}, \boldsymbol{R}_1]$, $[\mathcal{P}_{inf}, \boldsymbol{R}_2]$.

3.3 Synthetic Environment Results

720 instances of the filter was ran, with 20 different process models (Sec. 3.2.3), against 6 sets of observations (Sec. 3.2.2) and under 6 configurations (Sec. 3.2.4). Each instance computed a sequence of 3D catheter shapes during 2000 time steps, that were compared to the ground truth.

For a state vector $\boldsymbol{X}$ of size 120, a framerate of 12 FPS was achieved. The most expensive part was the computation of the collision response, which must be performed 121 times per time-step: one for each sigma-point.

This synthetic validation aimed at demonstrating how our approach can handle an ample range of model uncertainty, while providing valid results within a reasonable range of filter parameters tuning.

3.3.1 Sensitivity to Model Uncertainty

The filter performances were assessed against the variation on μ. Fig. 9 reports example results on the side view, with an observation noise covariance $\boldsymbol{R}_1$ according to different filter parameterizations: each graph corresponds to a different value of μ. The filter was able to provide an accurate estimate of the 3D catheter shape, even for extreme model uncertainties (i.e. $\mu = 0$, or $\mu = 0.08$). Errors were mainly noticeable in the depth direction and on the proximal part of the catheter (Fig. 9 (a-c)), meaning that the distal segment was always accurately reconstructed (Fig. 9 (d-i)). For a given observation data set and filter configuration, all the reconstructions presented the same error trend, indicating a behavior independent from model uncertainty. Nevertheless, the filter parameters $\mathcal{P}_{inf}$ provided the best results. The initial peak, common to all the graphs, is due to the filter starting-up. The effect of mechanical constraints on the quality of the reconstruction is particularly noticeable on Hausdorff distance that improves and stabilizes after the first contact (around $T = 250$). On average, we measured a 3D Hausdorff distance of 0.07 ± 0.37 mm; a 3D distance at the tip equal to 0.021 ± 0.009 mm and a 3D mean distance on the distal segment of the catheter of 0.02 ± 0.008 mm.

3.3.2 Sensitivity to Filter Parameter Tuning and Observations

The results of the filter were compared under the 6 different model parameterizations. Given the independence on the reconstructions against μ, the results were averaged over all values of μ. Fig. 10 reports the results measured using the side

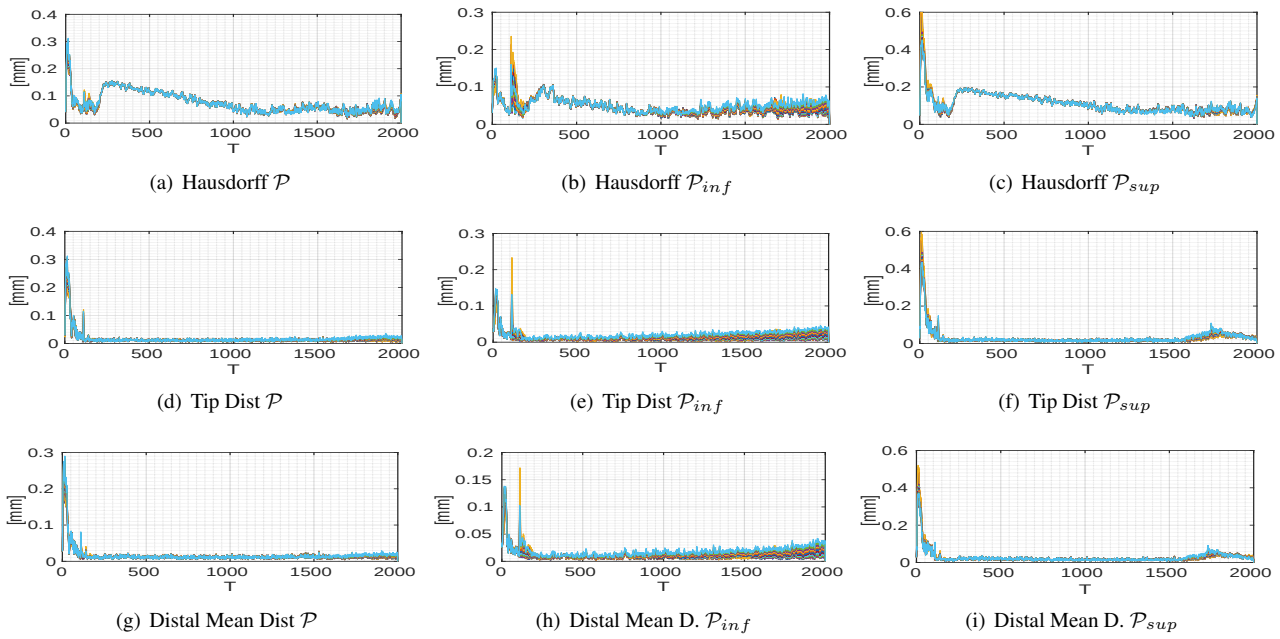

(a) Hausdorff $\mathcal{P}$ (b) Hausdorff $\mathcal{P}_{inf}$ (c) Hausdorff $\mathcal{P}_{sup}$

(d) Tip Dist $\mathcal{P}$ (e) Tip Dist $\mathcal{P}_{inf}$ (f) Tip Dist $\mathcal{P}_{sup}$

(g) Distal Mean Dist $\mathcal{P}$ (h) Distal Mean D. $\mathcal{P}_{inf}$ (i) Distal Mean D. $\mathcal{P}_{sup}$

Fig. 9. **Sensitivity to Model Uncertainty**. Comparing metrics for different process model parameterization (21 curves on each plot). Observations from the side view were used and measurement noise covariance was $\mathbf{R}_1$. All reconstructions lay within the same range of accuracy showing the same trends, independent of the uncertainty on the model (error on μ).

view. Reconstructed shapes are very accurate but tend to be noisier when the observation noise level is underestimated ($\boldsymbol{R}_2$ case): smaller values for the observation noise covariance imply a tendency to overtrust the observations, which means being more sensitive to erroneous data. The parameter sets $[\mathcal{P}_{sup}, \boldsymbol{R}_2]$ and $[\mathcal{P}, \boldsymbol{R}_2]$ provide less precise results against the other configurations, even though still below 0.4 mm (Fig. 10(c)).

The dependence on the observation view and filter configuration was also assessed. Fig. 11 reports our results for both side and top views, against filter model configurations $\mathcal{P}, \mathcal{P}_{sup}$ and $\mathcal{P}_{inf}$, combined with $\boldsymbol{R}_1$ covariance on the observations. Although $\mathcal{P}_{inf}$ setting (blue graphs) performed best, again, all tunings provided accurate results, for both acquisition views.

3.4 Experiments on Real Data

3.4.1 Ground Truth Reference

The real data-set was acquired using the testbed described in [31]. A 1.7F micro-catheter (Headway TM 17, MicroVention Inc.) was inserted in a rigid phantom made of a silicon mould of an internal carotid artery (H+N-R-A-003 model, Elastrat). This navigation within the transparent phantom was captured at 198 frames per second by a pair of two high speed cameras (TM-6740CL, JAI/Pulnix), synchronized using a trigger (C320 Machine Vision Trigger Timing Controller, Gardasoft). The stereovision camera setup was calibrated using a chessboard target and OpenCV algorithms. One camera was placed above the phantom, to provide a top view, and the other one provided the side view. In particular, the calibration measured the projection matrices for each view (matrix $\mathbf{C}$ in Eq. (22)).

A sequence of 2130 images (10.75 s) was acquired: the catheter was automatically segmented and reconstructed in 3D by triangulation in each frame. This provided the ground truth reconstruction. The reconstruction error was estimated to be below 0.05 mm on 1000 images of a motionless catheter. In this sequence, a stick and slip transition occurred around frame number $T = 1300$ (see Fig. 13, (f)-(h)). The speed of the catheter tip was estimated to peak at 500 mm/s in the slip phase.

3.4.2 FE model parameterization and 2D Observations

The catheter length was 6 cm at the end of the insertion. Thereafter, the catheter was modeled as a series of 11 connected beams, of 55 mm each (12 nodes). Without further knowledge on the physical properties of the material used (silicon, catheter, slippery liquid infused in the phantom...) the friction coefficient was set to $\mu = 0.1$ and the insertion forces was set according to the velocity values provided for the catheter motion in [31].

The detection of markers is out of the scope of this paper. Furthermore, the catheter did not carry any visible marker in the images. The 2D observations were therefore generated in a similar way as in the synthetic setup: virtual markers were placed along the ground truth shapes and reprojected in each frame, a Gaussian noise (with standard deviation of 0.1 pixel) was added to their locations.

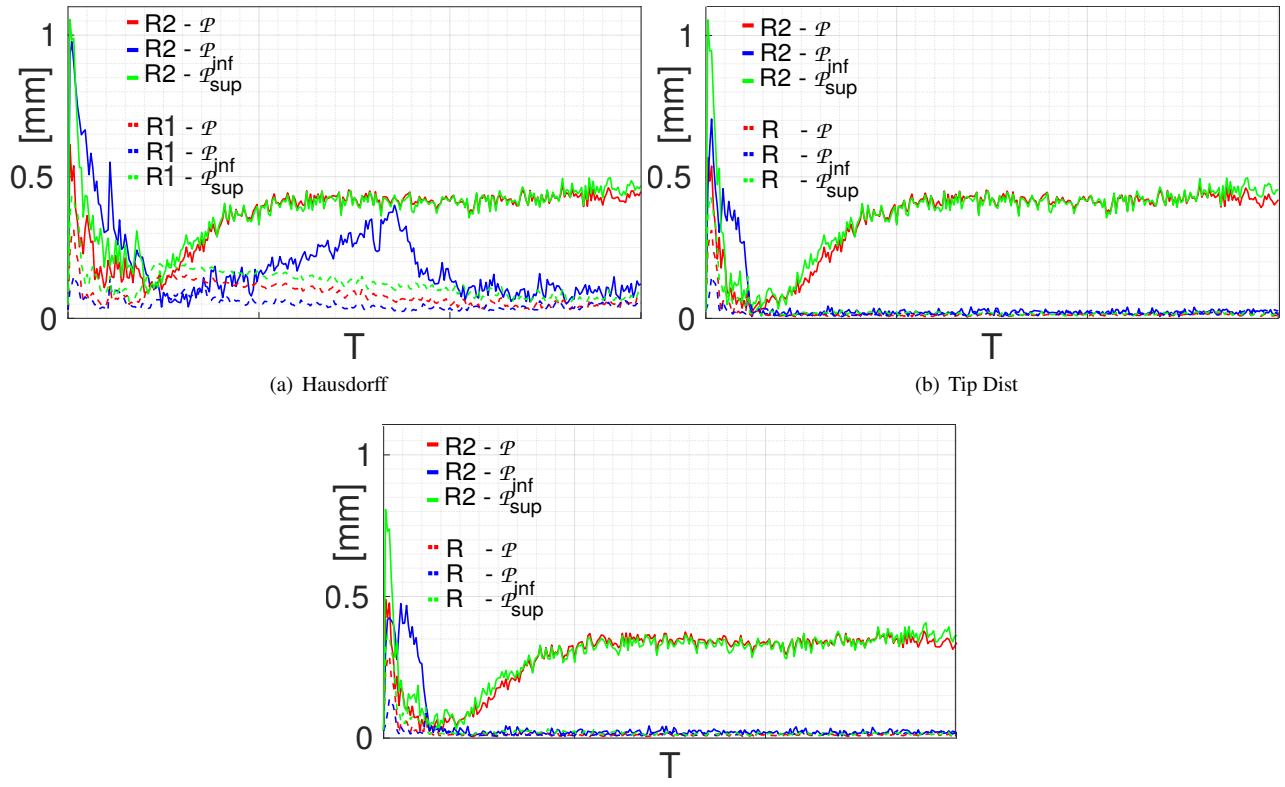

(a) Hausdorff (b) Tip Dist

(c) Distal Mean D.

Fig. 10. **Sensitivity to filter configuration**. Comparing shapes recovered from observations in the side view, using the 6 different filter parameterizations. Noisier shapes are reconstructed when the observation noise level is underestimated.

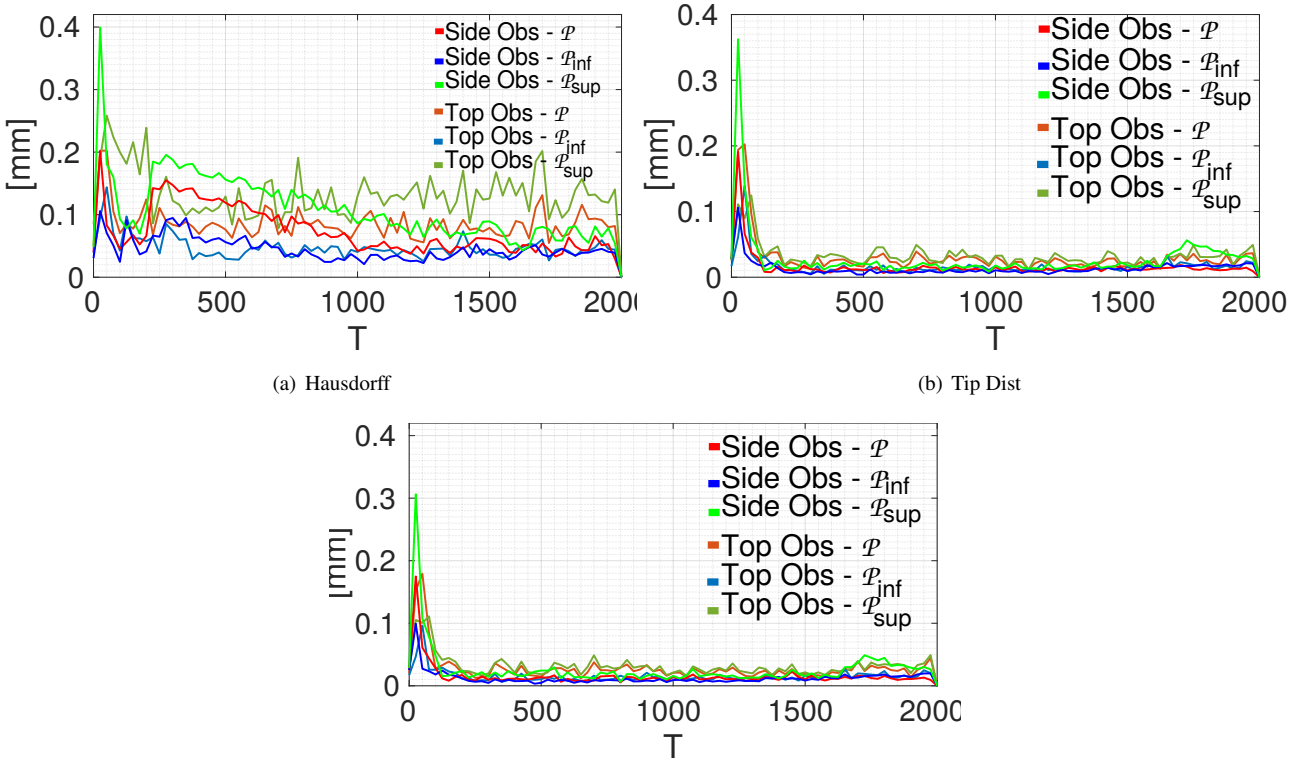

(a) Hausdorff (b) Tip Dist

(c) Distal Mean Distance

Fig. 11. **Sensitivity to view against filter configuration (model part)**. Hausdorff distance, tip and Distal Mean D.ances for both side and top observation views. Results are compared for filter configurations $[\mathcal{P}_{sup}, \mathbf{R}_1]$, $[\mathcal{P}, \mathbf{R}_1]$, $[\mathcal{P}_{inf}, \mathbf{R}_1]$, taking the average of all the model configurations respect to μ

3.4.3 Stochastic Environment: Filter Parameter Tuning

In this experiment, in order to accelerate the computation time, we used the reduced state vector with 9 components per node (no orientation, see Sec. 2.4.4).

Contrary to the synthetic environment, we had no precise knowledge of the process model. Instead, the nominal filter parameters $\mathcal{P}$ were set according to the diameter of the vessel ($\sim$ 6 mm): for positions $\sigma_{\mathbf{x}_{mod}} = 10^{-3}$ m, and for velocities $\sigma_{\mathbf{v}_{mod}} = [10^{-3}$ m/s, 10^{-3} rad/s] to account for a slower motion of the catheter by the operator than in the synthetic experiment. Filter instances were also run with higher and lower configurations $\mathcal{P}_{sup} = 1.75^2\mathcal{P}$ and $\mathcal{P}_{inf} = 0.25^2\mathcal{P}$. Three levels of observation noise covariance were also considered with $\sigma_{obs} \in \{0.1, 0.01, 0.001\}$ pixels (resp. denoted $\boldsymbol{R}_1$, $\boldsymbol{R}_2$ and $\boldsymbol{R}_3$).

3.5 Real Data Results

3.5.1 Filter parameterization

Fig. 12 reports the evaluation metrics between the retrieved shape and the ground truth, for different filter parameters. Only the average 3D distance on the distal segments is displayed, but all the metrics presented similar behaviors. All the configurations present a peak around $T \sim 1300$. This is due to the filter response to the stick and slip transition, a phenomenon where the cumulative effect of the friction force causes an abrupt movement of the device. The filter was able to rapidly recover from such a sudden variation in positions and velocities.

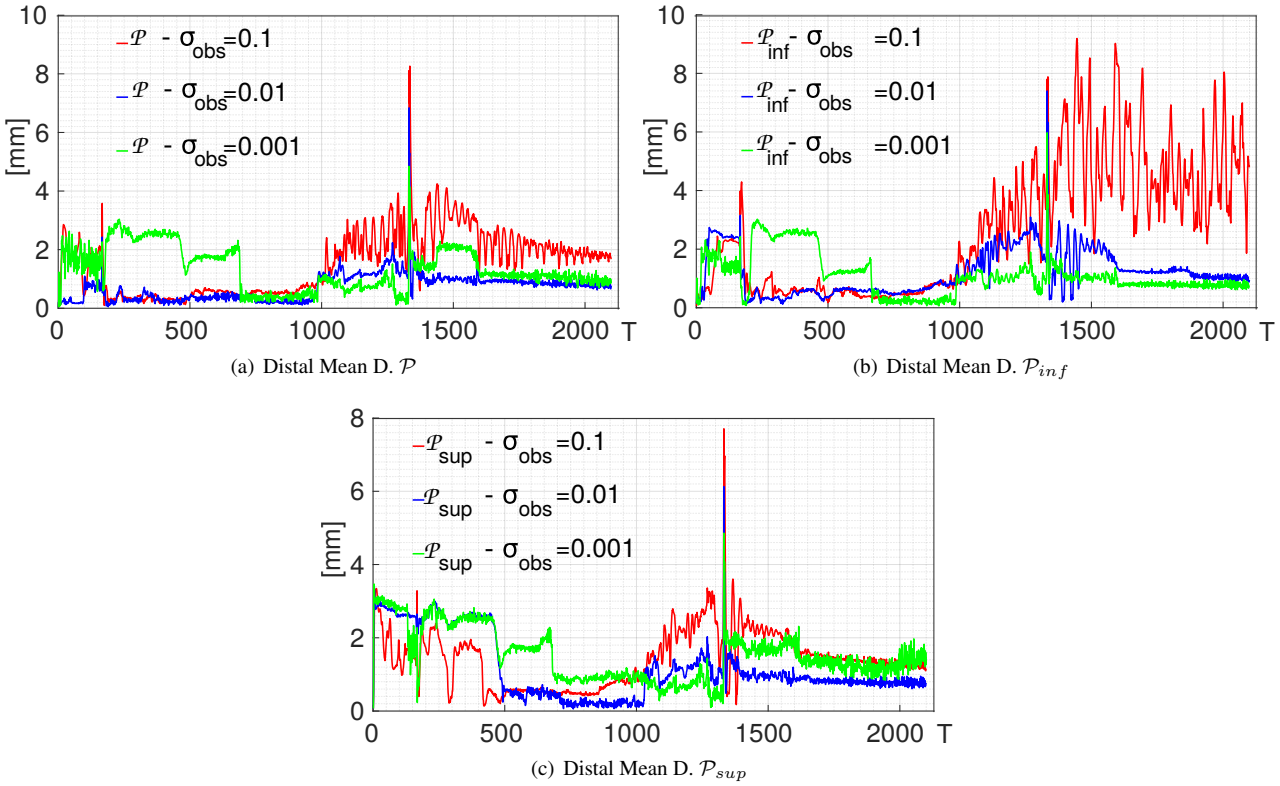

(a) Distal Mean D. $\mathcal{P}$

(b) Distal Mean D. $\mathcal{P}_{inf}$

(c) Distal Mean D. $\mathcal{P}_{sup}$

Fig. 12. **Sensitivity to Filter Tuning with real data**. Comparing reconstructed shapes with ground truth for different combinations of filter parameters. Trends are the same for all the settings; the peak error around T∼1300 is due to a rapid stick and slip transition.

Using the nominal parameter set $\mathcal{P}$, the filter response was quite robust to variations in the level of observation noise (Fig. 12 (a)). The reconstruction was noisier with the largest observation noise ($\sigma_{obs} = 0.1$ pixels), and the best for $\sigma_{obs} = 0.01$ pixels. This was common to all model configurations (see Fig. 12 (b) for $\mathcal{P}_{inf}$ and Fig. 12 (c) for $\mathcal{P}_{sup}$). When the model was too constrained ($\mathcal{P}_{inf}$ setting) in combination with too high a level of noise ($\sigma_{obs} = 0.1$ pixels), the filter could not recover from the stick and slip transition (red graph on Fig. 12 (b)). On the other hand, overtrusting the observations ($\sigma_{obs} = 0.001$ pixels, green graphs on all plots of Fig. 12) led to a longer recovery period after the stick and slip transition, but also to difficulties to adjust at the beginning of the navigation: it is interesting here to notice that the stabilization occurred at $T \sim 700$, which corresponds to the moment when the catheter was in contact with the vessel wall in 2 locations (see Fig. 13 (c) and (d)). This is an illustrative example of how contacts help constrain the ill-posed monocular reconstruction problem.

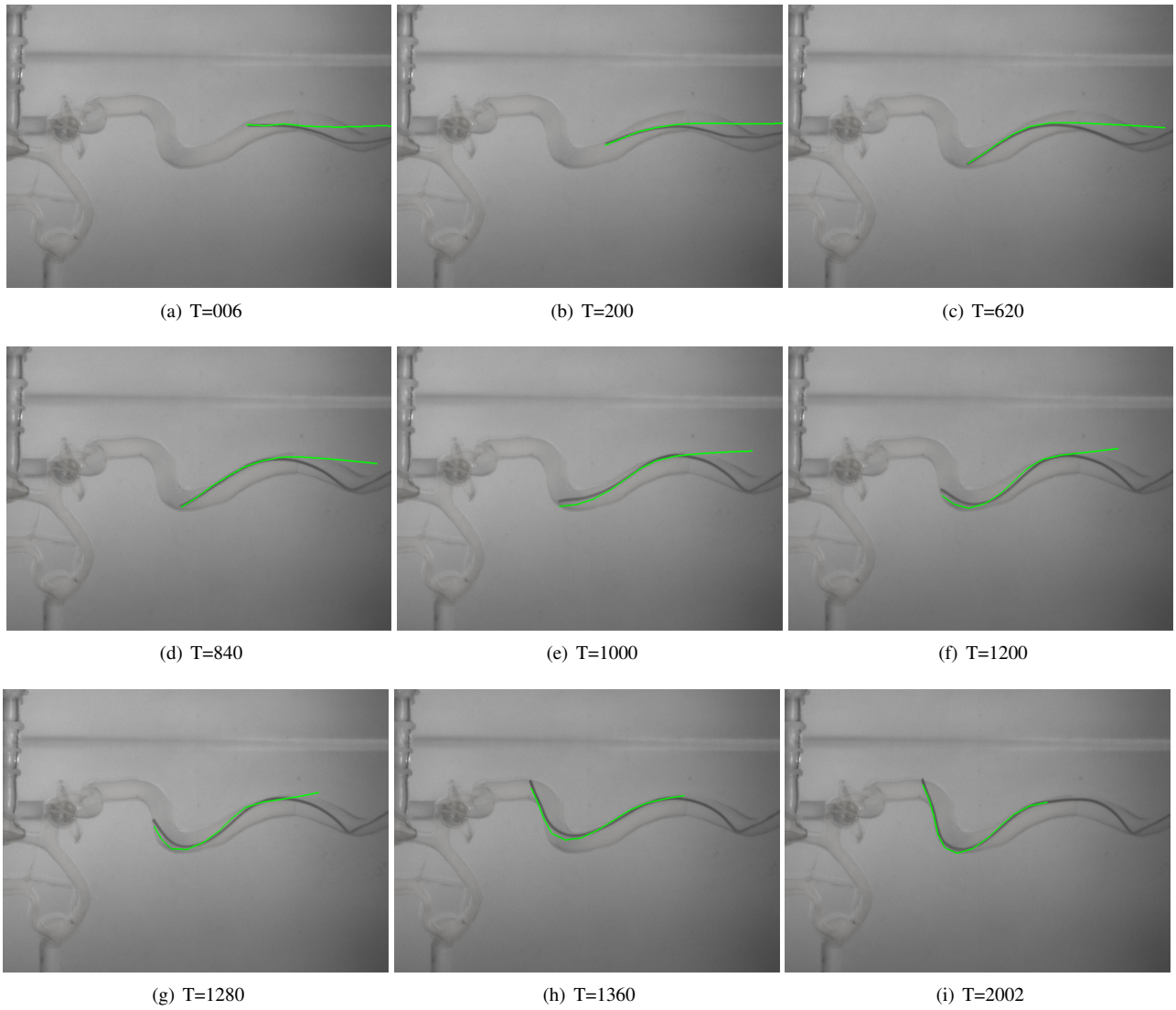

(a) T=006 (b) T=200 (c) T=620

(d) T=840 (e) T=1000 (f) T=1200

(g) T=1280 (h) T=1360 (i) T=2002

Fig. 13. **Qualitative Validation** The reconstructed shapes are superimposed in a view orthogonal to the observation view, with optimal filter configuration $\mathcal{P}, \sigma_{obs} = 0.01$ pixels. In fig. (f), (g), (h) it is possible to observe the stick and slip transition where an abrupt movement happens within a short interval (for more details see [31]

Overall, the best filter configuration combined $\mathcal{P}$ and $\sigma_{obs} = 0.01$ pixels, with an average Hausdorff distance of 0.95 $\pm$ 0.3559 mm, an average 3D distance at the tip equal to 0.7 $\pm$ 0.45 and an average 3D distance at the distal segment equal to 0.7 $\pm$ 0.46 mm. Fig. 13 presents qualitative reconstruction results: the side view was used for the observation data (observation view), and the reconstructed catheter is here superimposed (in green) over the top view (validation view, orthogonal to the observation view), to demonstrate how the physics-based constrained simulation helps to accurately recover the depth of the catheter relative to the observation view (vertical direction in the images).

3.5.2 Reducing the number of markers

Our method relies on the presence of opaque markers placed along the catheter. This is not the case for most current catheters. Therefore, we present here some preliminary results when the number of markers is reduced. For simplicity, we kept the one to one mapping between the markers and nodes, thereby allowing us to investigate faster versions of the filter with smaller state vectors.

When the number of observations was divided by two (6 markers/nodes, see Fig. 14), the filter could reconstruct the catheter when its motion was smooth and gradual. However, a loss of accuracy was observed after the stick and slip transition. Indeed, fewer observations, especially along the distal segment, entails a loss of information on the curvature of the device, which is extremely flexible and may undergo important deformations, like during the slip and stick transitions. This was confirmed when further reducing the number of markers/nodes down to 3 (Fig. 15). The sparsity of the observations implies

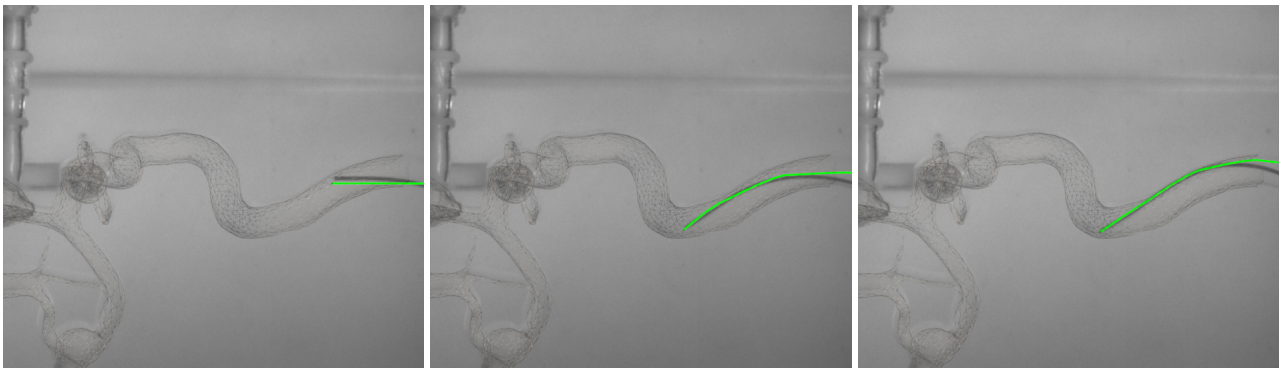

(a) T∼110 (b) T∼400 (c) T∼800

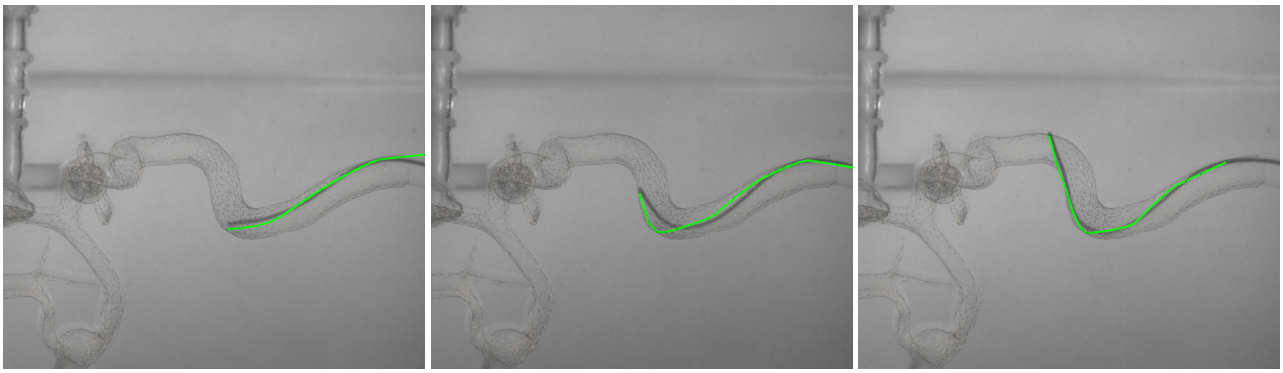

(d) T∼1000 (e) T∼1200 (f) T∼1700

Fig. 14. **Validation view using 6 observations**. Reconstruction appears less smooth compared to the background real image.

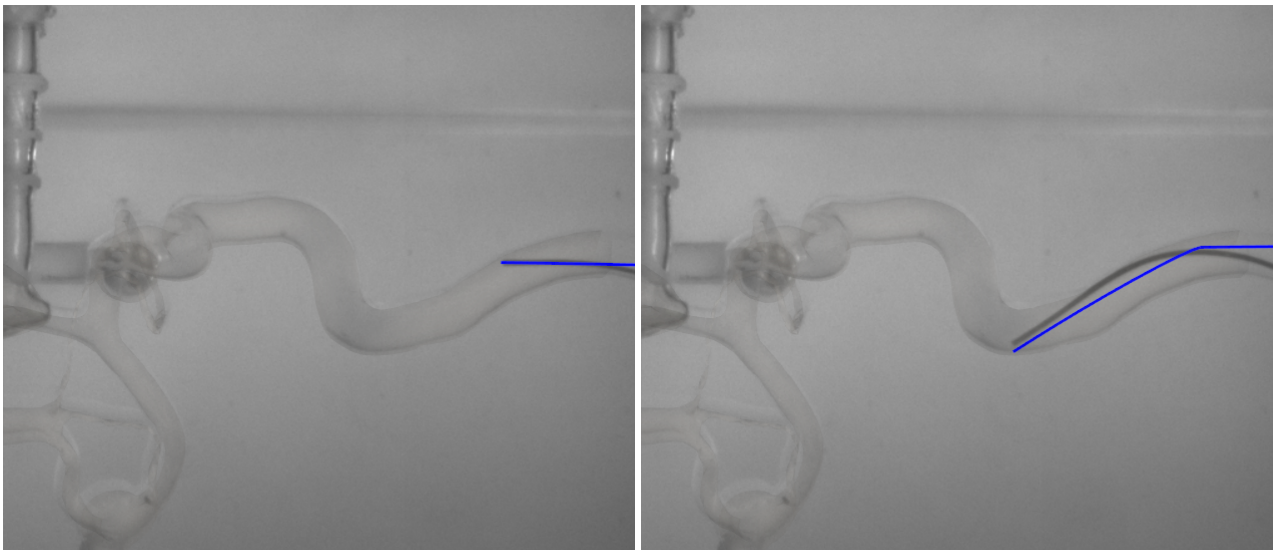

(a) T∼110 (b) T∼400

Fig. 15. **Validation view using 3 observations**. Such configuration does not allow to retrieve the correct curvature of the device

a lack of information about the bending of the device, which does not allow the filter to retrieve the correct 3D shape of the device. In conclusion, the number of observed markers depends on the rigidity of the device and the deformations it will be subject to. More rigid devices, like needles, could be reconstructed from a very small number of observations. But in the case of a catheter, a good design would probably adapt the number of markers to both the flexibility and the accuracy required by the application, and would therefore position more markers on the distal segment, and only a few markers on the proximal portion. Concerning computation time, we were able to reach up to 18 FPS, given the reduced state vector size and

the non estimation of nodal orientations.

4 Discussion and Conclusion

In a very common routine practice, interventional radiologists navigate catheters and guidewires through the vascular network under the visual guidance of single plane fluoroscopy images. This implies for the radiologist to infer the 3D shape of the device from a monocular view, which has been long known to be an ill-posed problem. Although recent progress in physics-based simulation have enabled realistic interactive virtual navigation, the 3D computed shape remains sensitive to even small uncertainties in the value of mechanical parameters, such as the friction coefficient.

To go beyond these limitations, we have proposed to embed a physics-based simulation in a Bayesian filtering framework where 2D observations are based on radio-opaque markers placed on the catheter detected in the fluoroscopic images. An Unscented Kalman Filter formulation is provided and was experimented in a synthetic setup and on real phantom data. Both quantitative and qualitative results demonstrate the ability of our method to recover an accurate 3D shape at interactive time frames, under a variety of filter parameterizations and challenging conditions: inaccurate friction coefficient and ambiguous views (synthetic scenario), non-linear complex contacts and abrupt stick and slip motions (real data set). The optimal filter parameterization could easily be deduced from practical considerations on the model uncertainty, but the standard deviation on the observation noise had to be underestimated by an order of magnitude. This question is part of our current investigations, but we believe that an offline calibration step could provide adequate values, to be used during the clinical procedure.

As presented in our results, we recently started to investigate the optimal markers/node configuration to reach the best compromise between practical setup, accuracy of the reconstruction, and simulation time. More in general, future works aim at improving the validation of our method to bring it closer to clinical application. For example, taking into account vessels deformability and displacements induced by patient's respiratory motion as well as improving the device insertion, providing a better description of the interventional radiologist's gesture.

References

[1] P. R. DeLucia, R. D. Mather, J. A. Griswold, S. Mitra, Toward the Improvement of Image-Guided Interventions for Minimally Invasive Surgery: Three Factors That Affect Performance, Human Factors: The Journal of the Human Factors and Ergonomics Society 48 (1) (2006) 23–38.

[2] S. Baert, E. van de Kraats, T. van Walsum, M. Viergever, W. Niessen, Three-dimensional guide-wire reconstruction from biplane image sequences for integrated display in 3-d vasculature, IEEE Transactions on Medical Imaging 22 (10) (2003) 1252–1258.

[3] C. Delmas, M.-O. Berger, E. Kerrien, C. Riddell, Y. Trousset, R. Anxionnat, S. Bracard, Three-dimensional curvilinear device reconstruction from two fluoroscopic views, in: SPIE, Medical Imaging 2015: Image-Guided Procedures, Robotic Interventions, and Modeling, Vol. 9415, San Diego, CA, United States, 2015, p. 94150F. doi:10.1117/12.2081885.
URL https://hal.inria.fr/hal-01139284

[4] S. Condino, V. Ferrari, C. Freschi, A. Alberti, R. Berchiolli, F. Mosca, M. Ferrari, Electromagnetic navigation platform for endovascular surgery: how to develop sensorized catheters and guidewires., The international journal of medical robotics and computer assisted surgery : MRCAS 8 (3) (2012) 300–10.

[5] S. Pujol, M. Pecher, J.-L. Magne, P. Cinquin, A virtual reality based navigation system for endovascular surgery., Studies in health technology and informatics 98 (2004) 310–2.

[6] A. Schwein, B. Kramer, P. Chinna Durai, S. Walker, M. O'Malley, A. Lumsden, J. Bismuth, Flexible Robotics With Electromagnetic Tracking Improve Safety and Efficiency During In Vitro Endovascular Navigation, Journal of Vascular Surgery 63 (1) (2016) 285–286.

[7] T. van Walsum, S. Baert, W. Niessen, Guide wire reconstruction and visualization in 3DRA using monoplane fluoroscopic imaging, IEEE Transactions on Medical Imaging 24 (5) (2005) 612–623.

[8] T. Petković, R. Homan, S. Lončarić, Real-time 3D position reconstruction of guidewire for monoplane X-ray, Computerized Medical Imaging and Graphics 38 (3) (2014) 211–223.

[9] M. Brückner, F. Deinzer, J. Denzler, Temporal estimation of the 3d guide-wire position using 2d X-ray images, Lecture Notes in Computer Science (including subseries Lecture Notes in Artificial Intelligence and Lecture Notes in Bioinformatics) 5761 LNCS (PART 1) (2009) 386–393.

[10] R. Trivisonne, E. Kerrien, S. Cotin, Augmented 3D Catheter Navigation using Constrained Shape from Template, in: Hamlyn Symposium, London, United Kingdom, 2017.

[11] A. Dore, G. Smoljkic, E. V. Poorten, M. Sette, J. V. Sloten, G. Z. Yang, Catheter navigation based on probabilistic fusion of electromagnetic tracking and physically-based simulation, in: IEEE International Conference on Intelligent Robots and Systems, 2012, pp. 3806–3811.

[12] A. Malti, R. Hartley, A. Bartoli, J. H. Kim, Monocular template-based 3d reconstruction of extensible surfaces with local linear elasticity, Proceedings of the IEEE Computer Society Conference on Computer Vision and Pattern Recognition (2013) 1522–1529.
[13] N. Haouchine, J. Dequidt, M. O. Berger, S. Cotin, Monocular 3D Reconstruction and Augmentation of Elastic Surfaces with Self-Occlusion Handling, IEEE Transactions on Visualization and Computer Graphics 21 (12) (2015) 1363–1376.
[14] A. Agudo, F. Moreno-Noguer, B. Calvo, J. M. Montiel, Real-time 3D reconstruction of non-rigid shapes with a single moving camera, Computer Vision and Image Understanding 153 (2016) 37–54.
[15] S. J. Julier, J. K. Uhlmann, New extension of the Kalman filter to nonlinear systems, in: Int. Symp. Aerospace/Defense Sensing, Simul. and Controls, 1997, pp. 182–193.
[16] R. E. Kalman, Others, A new approach to linear filtering and prediction problems, Journal of basic Engineering 82 (1) (1960) 35–45.
[17] R. Brown, P. Hwang, Introduction to Random Signals and Applied Kalman Filtering with MatLab Excercises Fourth Edition, Wiley, 2011.
[18] S. Timoshenko, LXVI.On the correction for shear of the differential equation for transverse vibrations of prismatic bars, The London, Edinburgh, and Dublin Philosophical Magazine and Journal of Science 41 (245) (1921) 744–746.
[19] C. A. Felippa, B. Haugen, A unified formulation of small-strain corotational finite elements: I. theory, Computer Methods in Applied Mechanics and Engineering 194 (21-24) (2005) 2285–2335.
[20] S. Cotin, C. Duriez, J. Lenoir, P. Neumann, S. Dawson, New approaches to catheter navigation for interventional radiology simulation., MICCAI 8 (2005) 534–542.
[21] D. Baraff, A. Witkin, Large steps in cloth simulation, Proceedings of the 25th annual conference on Computer graphics and interactive techniques - (SIGGRAPH '98) (1998) 43–54.
[22] C. Duriez, F. Dubois, A. Kheddar, C. Andriot, Realistic Haptic Rendering of Interactive Deformable Objects in Virtual Environments, IEEE Transactions on Visualization and Computer Graphics 12 (1) (2006) 36–47.
[23] H. Courtecuisse, J. Allard, P. Kerfriden, S. P. Bordas, S. Cotin, C. Duriez, Real-time simulation of contact and cutting of heterogeneous soft-tissues, Medical Image Analysis 18 (2) (2014) 394–410.
[24] P. Ambrosini, D. Ruijters, W. J. Niessen, A. Moelker, T. van Walsum, Fully automatic and real-time catheter segmentation in x-ray fluoroscopy, CoRR abs/1707.05137. arXiv:1707.05137.
URL http://arxiv.org/abs/1707.05137
[25] N. Honnorat, R. Vaillant, N. Paragios, Graph-based geometric-iconic guide-wire tracking, in: G. Fichtinger, A. Martel, T. Peters (Eds.), Medical Image Computing and Computer-Assisted Intervention – MICCAI 2011, Springer Berlin Heidelberg, Berlin, Heidelberg, 2011, pp. 9–16.
[26] Y. Wang, T. Chen, P. Wang, C. Rohkohl, D. Comaniciu, Automatic Localization of Balloon Markers and Guidewire in Rotational Fluoroscopy with Application to 3D Stent Reconstruction, in: Computer Vision – ECCV 2012, Springer Berlin Heidelberg, 2012, pp. 428–441.
[27] S. Gorges, E. Kerrien, M. Berger, Y. Trousset, J. Pescatore, R. Anxionnat, L. Picard, S. Bracard, 3D augmented fluoroscopy in interventional neuroradiology: Precision assessment and first evaluation on clinical cases, Workshop on Augmented environments for Medical Imaging and Computer-aided Surgery-AMI-ARCS 2006 (2006) 11–06.
[28] P. Moireau, D. Chapelle, Reduced-order Unscented Kalman Filtering with application to parameter identification in large-dimensional systems, ESAIM: Control, Optimisation and Calculus of Variations 17 (2) (2011) 380–405.
[29] R. Kandepu, L. Imsland, B. A. Foss, Constrained state estimation using the unscented kalman filter, 2008 Mediterranean Conference on Control and Automation - Conference Proceedings, MED'08 (2008) 1453–1458doi:10.1109/MED.2008.4602001.
[30] K. Takashima, R. Shimomura, T. Kitou, H. Terada, K. Yoshinaka, K. Ikeuchi, Contact and friction between catheter and blood vessel, Tribology International 40 (2) (2007) 319–328.
[31] M. Sanz-Lopez, J. Dequidt, E. Kerrien, C. Duriez, M.-O. Berger, S. Cotin, Testbed for assessing the accuracy of interventional radiology simulations, in: ISBMS - 6th International Symposium on Biomedical Simulation, LNCS, Springer, Strasbourg, France, 2014.